The Astrophysical Journal, 993:13 (19pp), 2025 November 1 https://doi.org/10.3847/1538-4357/ae018c

FEAST: JWST Uncovers the Emerging Timescales of Young Star Clusters in M83

Alice Knutas[1,2], Angela Adamo[1], Alex Pedrini[1], Sean T. Linden[3], Varun Bajaj[4], Jenna E. Ryon[4], Benjamin Gregg[5], Ahmad A. Ali[6], Eric P. Andersson[7], Arjan Bik[1], Giacomo Bortolini[1], Anne S. M. Buckner[8], Daniela Calzetti[5], Ana Duarte-Cabral[8], Bruce G. Elmegreen[9], Helena Faustino Vieira[1], John S. Gallagher[10], Kathryn Grasha[11,12,18], Kelsey Johnson[13], Thomas S.-Y. Lai[14], Drew Lapeer[5], Matteo Messa[15], Göran Östlin[1], Elena Sabbi[16], Linda J. Smith[4], and Monica Tosi[17]

[1] Department of Astronomy, Oskar Klein Centre, Stockholm University, AlbaNova University Center, SE-106 91 Stockholm, Sweden; angela.adamo@astro.su.se
[2] Department of Space, Earth and Environment, Chalmers University of Technology, SE-412 93, Göteborg, Sweden
[3] Steward Observatory, University of Arizona, 933 N Cherry Avenue, Tucson, AZ 85721, USA
[4] Space Telescope Science Institute, 3700 San Martin Drive, Baltimore, MD 21218, USA
[5] Department of Astronomy, University of Massachusetts, 710 North Pleasant Street, Amherst, MA 01003, USA
[6] I. Physikalisches Institut, Universität zu Köln, Zülpicher Str. 77, 50937 Köln, Germany
[7] Department of Astrophysics, American Museum of Natural History, 200 Central Park West, New York, NY 10024, USA
[8] Cardiff Hub for Astrophysics Research and Technology (CHART), School of Physics & Astronomy, Cardiff University, The Parade, CF24 3AA Cardiff, UK
[9] Katonah, NY 10536, USA
[10] Dept. Astronomy, U. Wisconsin, 475 North Charter Street, Madison, WI 53706, USA
[11] Research School of Astronomy and Astrophysics, Australian National University, Canberra, ACT 2611, Australia
[12] ARC Centre of Excellence for All Sky Astrophysics in 3 Dimensions (ASTRO 3D), Australia
[13] Department of Astronomy, University of Virginia, Charlottesville, VA, USA
[14] IPAC, California Institute of Technology, 1200 E. California Boulevard, Pasadena, CA 91125, USA
[15] INAF—OAS, Osservatorio di Astrofisica e Scienza dello Spazio di Bologna, via Gobetti 93/3, I-40129 Bologna, Italy
[16] Gemini Observatory/NSFs NOIRLab, 950 N. Cherry Avenue, Tucson, AZ 85719, USA
[17] INAF—Osservatorio di Astrofisica e Scienza dello Spazio di Bologna, via Piero Gobetti 93/3, 40129 Bologna, Italy
Received 2025 May 7; revised 2025 August 8; accepted 2025 August 19; published 2025 October 22

Abstract

We present JWST NIRCam observations of the emerging young star clusters (eYSCs) detected in the nearby spiral galaxy M83. The NIRcam mosaic encompasses the nuclear starburst, the bar, and the inner spiral arms. The eYSCs, detected in Paα and Brα maps, have been largely missed in previous optical campaigns of young star clusters (YSCs). We distinguish between eYSCI, if they also have compact 3.3 μm polycyclic aromatic hydrocarbon (PAH) emission associated with them, and eYSCII, if they only appear as compact Paα emitters. We find that the variations in the 3.3 μm PAH feature are consistent with an evolutionary sequence where eYSCI evolve into eYSCII and then optical YSCs. This sequence is clear in the F300M−F335M (tracing the excess in the 3.3 μm PAH feature) and the F115W−F187N (tracing the excess in Paα) colors, which become increasingly bluer as clusters emerge. The central starburst stands out as the region where the most massive eYSCs are currently forming in the galaxy. We estimate that only about 20% of eYSCs will remain detectable as compact YSCs. Combining eYSCs and YSCs ($\leqslant$10 Myr), we recover an average clearing timescale of 6 Myr in which clusters transition from embedded to fully exposed. We see evidence of shorter emergence timescales ($\sim$5 Myr) for more massive ($>5\times10^3$ $M_\odot$) clusters, while star clusters of $\sim10^3$ $M_\odot$ about 7 Myr. We estimate that eYSCs remain associated with the 3.3 μm PAH emission for 3–4 Myr. Larger samples of eYSC and YSC populations will provide stronger statistics to further test environmental and cluster mass dependencies on the emergence timescale.

Unified Astronomy Thesaurus concepts: Young star clusters (1833); Star forming regions (1565); Polycyclic aromatic hydrocarbons (1280)

1. Introduction

Young star clusters (YSCs) in local galaxies are primary tracers carrying information about the early phases and key mechanisms governing star formation. They are the main birthplaces of massive stars ($M > 8$ $M_\odot$; M. S. Oey et al. 2004) and therefore the primary source of stellar feedback, which plays a crucial role in regulating the star formation cycle and the evolution of their host galaxy (T. Naab & J. P. Ostriker 2017).

Most stars form in star clusters, but only some of those clusters are gravitationally bound; the large majority consists of stellar associations that will dissolve within a few crossing times (S. F. Portegies Zwart et al. 2010; M. R. Krumholz et al. 2019). At early stages, because of the clustered nature of star formation, it remains impossible to distinguish between bound star clusters and associations (A. Adamo et al. 2020), even in the solar neighborhood (E. Bressert et al. 2010). Thus, unless otherwise specified, we will use the term "star cluster" for young (<10 Myr) and compact stellar systems of which only a fraction is gravitationally bound and has a higher likelihood to survive in their host galaxies.

Star clusters are formed by the gravitational collapse of a giant molecular cloud (GMC; S. N. Longmore et al. 2014). Initially, the collapse produces dense cores, evolving into multiple protostars that resemble young stellar objects (YSOs) deeply embedded in their natal cloud (R. A. Gutermuth et al. 2011). Subsequently, feedback from massive stars ionizes the gas and creates an expanding H II region surrounded by an

[18] ARC DECRA Fellow.

interface layer, i.e., a photodissociation region (PDR) followed by the remaining molecular gas of the GMC (D. Hollenbach & A. Tielens 1997). During this phase, stars emerge from their natal cloud to become partly embedded and later fully exposed. The most embedded clusters are typically observed in millimeter, radio, and infrared (e.g., H. A. Kobulnicky & K. E. Johnson 1999; K. E. Johnson et al. 2003; A. E. Reines et al. 2008; D. G. Whelan et al. 2011), while the emerging ones become increasingly visible at shorter wavelengths, for example, near-IR (NIR) and optical. A fully exposed cluster is observed at ultraviolet (UV)-optical wavelengths. In this paper, we will refer to the timescale for a cluster to become fully exposed as the *emerging timescale*. The zero-point of this sequence is assumed to be the detection of NIR H emission lines (e.g., Paα), implicitly requiring that massive stars have reached the main sequence and are capable of ionizing their circumstellar material. We define all clusters along this evolutionary phase as emerging YSCs (eYSCs).

Several studies conducted in Milky Way star-forming regions have revealed that eYSCs are associated with the presence of both H recombination lines and IR emission due to reprocessed far and near-UV photons by dust grains and polycyclic aromatic hydrocarbons (PAHs) in PDRs (E. Churchwell et al. 2009). Before the advent of JWST, the study of eYSCs at high resolution in nearby galaxies was mainly performed using Hα emission mapped with the Hubble Space Telescope (HST). The Hα morphological appearance (from compact to open H II regions) has been used to map the gradual emergence phase of star clusters (e.g., B. C. Whitmore et al. 2011). Using cluster age dating obtained from spectral energy distribution (SED) fitting, the emerging timescales appear to last between 4 and 5 Myr (K. Hollyhead et al. 2015; S. Hannon et al. 2019), but could be as fast as 2 Myr (S. Hannon et al. 2022), for clusters in the range of $M \sim 10^{2.5}$–$10^{3.5}\,M_{\odot}$. However, up to 60% of YSCs (ages of 1–6 Myr) are missed in optical and UV surveys, and only detected at IR wavelengths (M. Messa et al. 2021; S. T. Linden et al. 2023), making these timescales unreliable. M. Messa et al. (2021) used the NIR coverage of HST, covering the Paβ emission line, and found that gas clearing starts after 3 Myr, and is completed by 5 Myr. More recently, T. McQuaid et al. (2024) and S. Deshmukh et al. (2024) reported similar results. Overall, these studies are limited to small number statistics (up to several tens of low-mass clusters, $\sim$1000 $M_{\odot}$). This raises the question of whether emerging timescales are different for more massive star clusters and/or vary as a function of galactic environment. Since the advent of JWST, we can directly observe embedded star clusters. In particular, the 3.3 μm PAH feature has been used to detect embedded massive YSCs (S. T. Linden et al. 2023; M. J. Rodríguez et al. 2023; B. C. Whitmore et al. 2023). For example, by crossmatching HST and JWST observations, B. C. Whitmore et al. (2023) reported a completely obscured phase lasting about 1.3 Myr and a partially obscured one lasting about 3.7 Myr. In the circumnuclear starburst ring of NGC 3351, J. Sun et al. (2024) have combined JWST, Atacama Large Millimeter/submillimeter Array (ALMA), and HST observations to sample the complete evolutionary sequence from the onset of dense molecular cores to young massive clusters ($\sim 10^5\,M_{\odot}$). They derived timescales of 2–4 Myr for the transition from the most embedded phase of dense molecular cores to NIR bright eYSCs and 4–6 Myr in total to become detectable at optical wavelengths.

In this work, we will analyze the eYSC population of the nearby star-forming galaxy M83 ($d = 4.7$ Mpc; R. B. Tully et al. 2013) using JWST NIRCam observations obtained under the Feedback in Emerging extragAlactic Star clusTers (FEAST; GO 1783, PI Adamo). M83, also known as NGC 5236, is a barred spiral galaxy with $\log_{10} M_{*} = 10.53$ $M_{\odot}$ (A. K. Leroy et al. 2021). It presents enhanced star formation along the spiral arms and the regions at the end of the bar (A. Adamo et al. 2015). The bar is responsible for feeding the circumnuclear starburst ring in the center (L. Della Bruna et al. 2022) where the most massive star clusters have been detected (J. Harris et al. 2001; A. Wofford et al. 2011). The FEAST JWST NIRCam mosaic covers roughly $6' \times 2'$, which in physical scale corresponds to about 8.2×2.7 kpc in the northeast direction (see Figure 1). We sample diverse galactic environments, the nuclear starburst, the bar, the end of the bar, and the spiral arms, including a good portion of the interarm area. In these regions, several works have reported variations in the physical properties of the GMCs and star clusters (A. Adamo et al. 2015; P. Freeman et al. 2017), as well as in the physical conditions of H II regions (L. Della Bruna et al. 2022). In this work, we present the observed and physical properties of the complete star cluster population younger than 10 Myr, including eYSCs, and estimate the emerging timescale as a function of galactic environment and cluster stellar mass.

The data set used in this work is presented in Section 2. In Section 3, we describe the method used to extract eYSCs. We present the demographics of this newly discovered cluster population and discuss how it relates to the physical properties of optically selected star clusters in Section 4. We provide estimates of emerging timescales in different galactic environments and as a function of cluster masses in Section 5. Our conclusions are presented in Section 6.

2. Observations and Data Reduction

We combined publicly available HST data and newly obtained JWST NIRCam observations of the inner $\sim$4 kpc of the disk of M83. Data reduction of HST and NIRCam observations of the FEAST targets will be presented in detail in A Pedrini et al. (2025). We provide here a short summary tailored to the observations acquired for M83.

HST observations were acquired with the Wide Field Camera 3 instrument (WFC3) under three programs: the WFC3 early release science program GO 11360 (PI Bob O'Connell), GO 12513 (PI Blair), and GO 17225 (PI Calzetti). In this study, all data available in the F275W, F336W, F438W, F547M, F555W, F657N, F689M, and F814W were downloaded from the MAST archive, reduced and drizzled into mosaics with a common pixel scale of $0\farcs04\,\mathrm{px}^{-1}$. The mosaics were registered to the Gaia reference system.

The galaxy was observed in eight JWST NIRCam bands sampling the stellar continuum and hot dust between 1 and 5 μm (F115W, F150W, F200W, F300M, F444W), H recombination lines such as Paα (F187N) and Brα (F405N), and the 3.3 μm PAH feature (F335M). A FULLBOX 4TIGHT primary dither pattern along with a subpixel dither pattern (STANDARD with two positions) was used, ensuring the coverage of a large field of view (FOV) $\sim 2\farcm2 \times 6'$ (see Figure 1) as well as a proper sampling of the NIRCam point-spread function

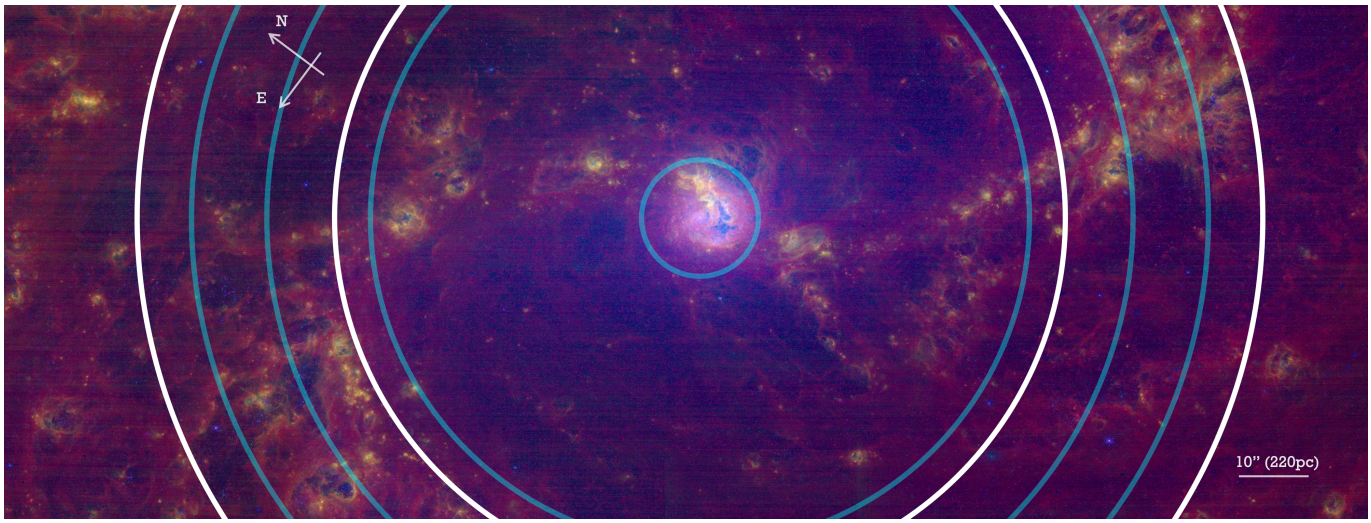

Figure 1. A three-color NIRCam composite image of the JWST field of view of M83, using the F115W (blue), F187N continuum-subtracted (green), and F335M continuum-subtracted (red). The white circles represent informed environmental regions as a function of galactocentric distance: the center, the bar, the end of the bar, and the outer regions. The light-blue circles have been obtained by dividing the galaxy into bins containing the same numbers of combined eYSCs and oYSCs. In this second division, we exclude the center (inner blue circle) and define the bar, the leading inner-bar region, the trailing outer-bar region, and the outer region (see Section 5.3).

(PSF). The NIRCam data were reduced using the JWST pipeline and the calibration reference files "`jwst_1174.pmap`". The Gaia registered F814W mosaic was used as an anchor to register the NIRCam F200W mosaic, which in turn was used as a reference to register the remaining NIRCam data. The final NIRCam mosaics have a common pixel scale of $0\farcs04$ pixel^{-1} and are in units of Jy pixel^{-1}.

2.1. Continuum-subtracted Maps

The JWST F187N, F405N, and F335M filters, which are tracers of Paα, Brα, and 3.3 μm PAH emission, respectively, capture a significant fraction of flux coming from stellar continuum and hot dust thermal emission. To account for this fraction, and to obtain final emission maps of these features, we estimated and subtracted the continuum emission from these filters using adjacent broad- and medium-band filters. We employed an iterative methodology to account for additional emission from these features in the adjacent filters. The reader may find an in-depth description of this process in B. Gregg et al. (2024), as well as a comprehensive discussion on the quality of the resulting maps. In summary, the Paα emission line map is obtained by subtracting stellar continuum emission using the F150W and the F200W filters. Conversely, we used F300M and F444W to estimate both maps of the 3.3 μm PAH feature and the Brα emission line. For each emission map, the detection limit is fixed at 5σ, where σ corresponds to the background rms value estimated during the point-like sources extraction process (see Section 3.1 and Appendix A). The 5σ limit is equal to 4×10^{-8}, 2×10^{-8}, and 1.8×10^{-8} Jy pixel^{-1} for Paα, Brα, and 3.3 μm PAH, respectively. For the Paα and Brα emission maps, the detection limits correspond to an emission rate of hydrogen ionizing photons, a $\log_{10}(Q_0) = 47.3$ photons per second. Indicatively, this Q_0 value is comparable to the brightness of the emission from an H II region with a circularized radius of 2 pc powered by an O9.5V spectral type star (R. C. Kennicutt 1998; B. T. Draine 2010).

Final science-ready mosaics and continuum-subtracted maps will be available at https://feast-survey.github.io.

3. Cluster Extraction and Photometry

As presented in Adamo et al. (2025, in preparation), we used two different approaches to achieve a complete census of the cluster population from embedded phases to optically bright systems that might survive several hundreds of megayears. This step was necessary as star clusters cover a large color range, making some clusters easier to detect in the NIR (emerging clusters, clusters with red supergiants), while others are easier to find in optical HST images (e.g., unobscured clusters).

3.1. The Optically Extracted YSC Population

We used our newly developed `FEAST-pipeline` to extract point-like sources in the HST F555W and F547M mosaics because they cover complementary regions of the galaxy (center and disk). The *V* band is typically used in HST optical studies of star cluster populations because it is less affected by extinction than UV bands and less prone to contamination by late stages of stellar evolution (e.g., red giants, etc.) affecting the IR bands (e.g., A. Adamo et al. 2017). We refer the reader to Adamo et al. (2025, in preparation) for a complete introduction of the FEAST-pipeline; here, we describe the main steps taken to produce the photometric catalogs. The extraction step is based on the `Source extraction and Photometry` (`SEP`) function (E. Bertin & S. Arnouts 1996; K. Barbary 2016). We used as parameters for the extraction a minimum of 5σ detection over 10 contiguous pixels, a background mesh of 30 pixels, a deblending parameter of 32, and a contrast of 0.0005 (see Table A1). Since the mosaics are all aligned, we allowed an improvement of the centering of each source only in the reference filter and used the final position for the next steps. Photometry of all HST and NIRCam bands was performed using an aperture radius of five pixels and a two-pixel-wide local sky annulus located at a radius of seven pixels. The

Table 1
Final Number of Sources in Each eYSC Class and Optical YSCs after Photometric Error Cuts Have Been Applied

Class	eYSCI	eYSCII	3.3 μm PAH Peaks	YSCs [FOV]
Photometric catalog	1126	453	403	7777 [3055]
# of candidates	946	361	389	3195 [829]

Note. We use this catalog to produce the observed IR colors of the eYSCs in Section 4. In the case of the optical YSC catalog, we report between brackets the number of cluster candidates within the NIRCam footprint. In the second row, we list the number of eYSCs and oYSCs (i.e., YSC with ages below 10 Myr) after crossmatching their positions, applying a $\chi^2_{\rm red} \leqslant 20$, and an age cut at 10 Myr in the case of oYSCs. We use these selected clusters in the analysis presented in Section 4.2.

concentration index (CI) of each extracted source was measured in the reference band (F555W or F547M) from the magnitude difference at a one- and three-pixel radius.

The aperture correction was derived from a reconstructed model of each star cluster where its approximate effective radius, $R_{\rm eff}$, has been taken into account. Analyses of star cluster populations in nearby galaxies (distance within 10 Mpc) find that YSC surface brightness profiles are better described by a Moffat (e.g., EFF; R. A. W. Elson et al. 1987) function with an average $R_{\rm eff} \sim 2$–3 pc and a power-law index of 1.5 (R. A. W. Elson et al. 1987; S. S. Larsen 2004; J. E. Ryon et al. 2015, 2017). In particular, J. E. Ryon et al. (2017) show a tight correlation between the $R_{\rm eff}$ and the CI of a star cluster. We therefore used the CI derived for each source in the reference filter (F555W or F547M in this case) to extrapolate the closest $R_{\rm eff}$, as follows. By construction, we built a grid of Moffat models with a fixed index of 1.5 and radii changing from 0 to 5 pc (converted in angular scales assuming the distance of the galaxy). These models have been convolved with the stellar PSF of the reference image, and CIs were then estimated in a similar fashion as for the observations. The extrapolated relation between CI versus $R_{\rm eff}$ in the reference filter was then used to associate with each source an $R_{\rm eff}$ from its CI. This means that, for each source, we established the closest Moffat model that described its light distribution. We then created the shape of the source in all the other bands by convolving this model to the PSF of each filter and estimated the aperture correction up to 20 pixels ($0\farcs8$).

In total, the initial extraction produced 78,427 sources for which photometry and a CI have been estimated. We selected among these objects those that were detected with a signal-to-noise ratio higher than 5 ($\sigma_{\rm err} \leqslant 0.2$ mag) in F438W, F547M or F555W, and F814W, and that were clearly distinct from massive single stars, i.e., that they have an absolute magnitude in V (F547M or F555W) of -6 ABmag (assuming a distance modulus of 28.34 mag), and a CI larger than 1.2 mag (the latter derived for the stellar PSF). This selection resulted in 13,467 sources over the entire FOV. Instead of visually inspecting this catalog from scratch to distinguish star cluster candidates from interlopers, we used the latest optical cluster catalog published by L. Della Bruna et al. (2022) as a starting point for the visual classification. The latter catalog includes 7459 cluster candidates, of which 7280 were published by A. Adamo et al. (2015), and 179 were newly detected in the inner area of radius 0.45 kpc of M83. This catalog contains cluster candidates flagged as "class 1" (compact extended sources), which we will refer to here as "class 1+2" following the LEGUS and PHANGS convention (A. Adamo et al. 2017; D. Maschmann et al. 2024), and "class 2" (multiple peaked, elongated objects) hereafter referred to as "class 3" in the convention adopted for the FEAST galaxies. Both the newly extracted FEAST catalog and the catalog of L. Della Bruna et al. (2022) were simultaneously visually inspected. The majority (7419 out of 7459) of L. Della Bruna et al.'s cluster candidates were confirmed in this updated inspection, and an additional 455 sources with compact appearance and diffuse light profile in their wings (corresponding to LEGUS "class1 +2") were found. In total, this visual inspection produced 7874 candidates. We repeated the photometry steps for these confirmed candidates allowing improving centering within one pixel in x- and y-directions in the reference band. The final FEAST photometric catalog of the optical clusters contains 7777 star cluster candidates after a 5σ selection on four HST broadbands (F336W, F438W, F555W or F547M, F814W) was applied (see Table 1). This catalog also includes a position flag "fov," which is set to 1 if the cluster is within the JWST FOV.

3.2. NIR-extracted eYSC Population

To detect eYSCs, we used the emission from the surrounding H II region and PDR as a signpost for the presence of a star cluster. We started from the JWST H recombination line maps: 1.87 μm Paα and 4.05 μm Brα tracing the H II region and the 3.3 μm PAH emission map tracing the PDR. The latter emission feature has already been shown to trace embedded star clusters (e.g., S. T. Linden et al. 2023; M. J. Rodríguez et al. 2023).

Using the `FEAST-pipeline`, we applied a similar procedure as for the extraction of the optical YSCs. The used extraction parameters are optimized to select compact sources and are listed in Table A1 in Appendix A. In total, 7010, 15,077, and 11,956 sources were extracted in the Paα, Brα, and 3.3 μm PAH maps, respectively.

To confirm the identified sources, we performed simultaneous visual inspection of the three catalogs in the respective emission line maps using SAOImageDs9 (W. A. Joye & E. Mandel 2003) as a supporting tool. The goal was to clean each catalog of residuals, recenter sources, add sources missed in the extraction, and remove sources that did not show a clear compact peak in emission in their respective emission maps. Before visual inspection, we applied a further selection to the 3.3 μm PAH extracted sources, which suffered from a severe contamination of residuals in the continuum-subtracted maps. To simplify the inspection process, we applied a magnitude and error cut at 21 mag and 0.1 mag, respectively. This step did not affect the final 3.3 μm PAH detections, as we included compact sources not accounted by the automatic extraction during visual inspection. To test this, we compared the range of magnitude distributions in F335M between the automatic source catalog and the final catalog after visual inspection and they covered similar ranges of luminosities, extending to fainter magnitudes than the applied cut.

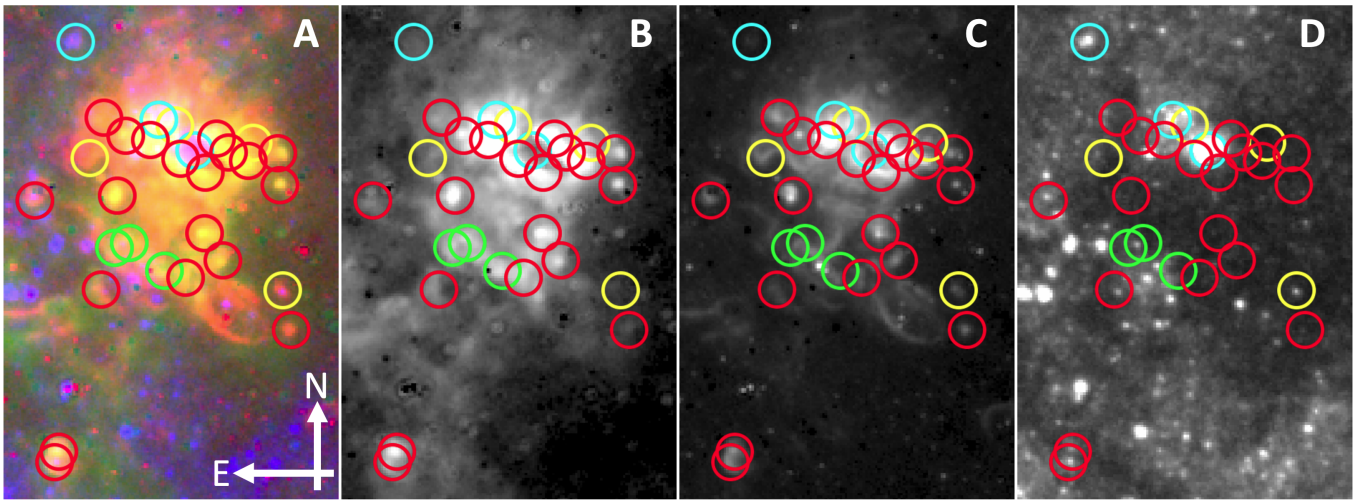

Figure 2. A three-color composite (panel (A)) of a giant star-forming complex in M83 (4.″6 × 8.″2 corresponding to a 105 × 195 pc): the green channel transmits the continuum-subtracted 3.3 μm PAH map (also shown in panel (B)); red: continuum-subtracted Paα map (panel (C))); blue: HST/F555W (panel (D))). Different classes of identified star clusters are overplotted as circles of a five-pixel radius (0.″28 corresponding to 6.4 pc), with eYSCI in red, eYSCII in yellow, 3.3 μm PAH peaks in green, and YSCs (younger than 10 Myr) in cyan. In the 3.3 μm PAH map, eYSCI and 3.3 μm PAH peak systems appear to have compact emission. The eYSCII sit in regions where 3.3 μm PAH emission is significant, but they are not associated with a compact morphology. In panel (C), eYSCI and eYSCII are clearly associated with compact Paα emission, while a compact counterpart is not seen in any of the 3.3 μm PAH peaks. In panel (D), optical YSCs with ages $\leqslant$10 Myr are associated with strong continuum emission, while that is not always the case with eYSCs, suggesting that the latter are significantly more reddened.

Next, we use the resulting visually confirmed sources in Paα, Brα, and 3.3 μm PAH maps to perform photometry with the `FEAST-pipeline`. For the eYSC candidates, we used the NIRCam F200W as a reference filter to estimate the aperture correction. We did not allow further centering to avoid misplacement due to proximity to bright sources. We extract photometry in all HST and JWST bands using an aperture radius of five pixels, and a two-pixel-wide sky annulus of a radius of seven pixels.

To distribute the visually vetted sources into different eYSC classes, we introduced an overlapping criterion among the three distinct catalogs. A source was considered to be the same object if it was identified across catalogs within a distance of four pixels ($\sim$3.6 pc). We tested this assumption by allowing instead an overlap of six pixels ($\sim$5.5 pc). The latter resulted in only 2%–5% variations in the identification of the same sources. Therefore, we opted for a criterion of four pixels to match the catalogs. During this step, we noticed that the Brα catalog resulted in fewer detections than in Paα due to the lower resolution of the map and shallower depth, which did not always allow us to deblend/detect sources clearly detected in the Paα map. Therefore, detection in the Brα map was not a necessary condition during the sorting of the classes. Sources detected as compact emission in Paα and 3.3 μm PAH catalogs (satisfying the above defined overlapping criterion) are referred to as eYSCI. Sources detected in Paα that did not have a compact counterpart emission in the 3.3 μm PAH catalog are named eYSCII. Finally, sources only detected in the 3.3 μm PAH catalog are referred to as 3.3 μm PAH peaks. We created final photometric catalogs for each class, where we listed the position and photometry of the Paα catalog for eYSCs detected in Paα and position and photometry of the 3.3 μm PAH catalog for the 3.3 μm PAH peaks. We included in the respective class catalogs only sources that have detection in NIRCam F187N, F200W, F335M, F405N, and F444W, with photometric errors lower than 0.3 mag. Table 1 reports the final number of sources in each class.

In Figure 2, we zoom in into a star-forming complex in the northeast spiral arm to visualize the different classes and emission properties. The coexistence of all classes is an indication of the complexity of star formation propagating in the region. The eYSCI have clear compact/peaked detection in the 3.3 μm PAH (panel (B)) and Paα (panel (C)) emission maps. The eYSCII have a compact emission in the Paα map, and are located in areas where diffuse 3.3 μm PAH emission is present, but not in a compact morphology that would identify an underlying powering star cluster. The 3.3 μm PAH peak is clearly identified in the 3.3 μm PAH map and is surrounded by diffuse Paα emission. Finally, we also include the optically detected YSCs (oYSCs) younger than 10 Myr extracted in the F555W filter. In panel (D), it is possible to see that oYSCs have strong continuum, while the majority of eYSCs and 3.3 μm PAH peaks are spatially located in dusty regions with no optical counterpart.

3.2.1. F200W Broadband Source Extraction

S. T. Linden et al. (2023) have proposed an alternative method to select eYSC candidates using only broad- and medium-band filters in the absence of narrowband emission line observations. We follow this alternative method here to extract potential eYSCs that are not associated with H recombination line emission. These could potentially be deeply embedded clusters or low-mass systems that have not sampled a massive enough star to power a H II region above our detection limits. We performed a blind source extraction in the F200W broadband using the `FEAST-pipeline` with the extraction parameters given in Table A1 in Appendix A and photometry parameters applied to estimate the photometry of the eYSCs presented above. We apply a magnitude cut that selects sources with a magnitude error below 0.2 in F335M, F150W, and F200W JWST bands to ensure a high signal-to-noise ratio. Additionally, to select potentially embedded clusters, we apply a CI cut for the F200W broadband larger than 1.2 mag and the color selection defined as F150W

−F200W > 0.48 mag and F200W−F335M > 0 mag (S. T. Linden et al. 2023). A comparison with the already extracted eYSCs shows that 70 eYSC candidates have been potentially missed in our extraction, that is, less than 5%. We discuss the recovered IR colors of these sources, referred to as eYSC-BB (eYSCs selected in broadband colors), in Section 4.1. Due to the small numbers and uncertain nature of these sources, we have decided not to include them in the SED analysis.

3.3. SED fitting

To analyze the SED of our samples of eYSCs and optical YSCs, and to investigate variations in their physical properties, we performed an SED-fitting analysis using the Code Investigating GALaxy Emission (CIGALE; M. Boquien et al. 2019). In Linden et al. (2025, in preparation) and A. Pedrini et al. (2025), we present in-depth analyses of the CIGALE-fitting methodology adopted within the FEAST program, as well as comparisons between different approaches and codes, and the reliability of the recovered physical properties of the star clusters. Here, we present a short summary of the fitting process. In a nutshell, CIGALE generates a wide grid of models that characterize the parameter space shaped by stellar, nebular, and dust contribution from a source, along with its star formation history. For star clusters, we considered a single burst of star formation with the exponential decay factor $\tau_{\rm burst} = 0.001$ Myr. We constrained the age of eYSCs to vary from 1 to 10 Myr, as these objects are selected to be bright in H recombination lines emission. On the other hand, we do not put any age restrictions for the optical clusters. The stellar emission grid uses G. Bruzual & S. Charlot's (2003) single stellar population, with G. Chabrier's (2003) initial mass function (IMF) and solar metallicity, while nebular grids are generated using CLOUDY (G. J. Ferland et al. 2013; M. Boquien et al. 2019). Dust emission models are from B. T. Draine et al. (2013). We account for dust attenuation using the CIGALE modified starburst model (see M. Boquien et al. 2019), which consists of a parametrized version of the starburst attenuation law (D. Calzetti et al. 2000). Moreover, the adopted parameter space allows the addition of a reduction factor between the attenuation computed from the emission lines and the stellar continuum attenuation. For the emission lines, we used the J. A. Cardelli et al. (1989) extinction curve. The full grid of models has been fitted for each eYSC and optical YSC candidate in our final photometric catalogs (see Table 1), using HST/WFC3 F225W, F275W, F336W, F438W, F547M, F555W, F657N, F689M, and F814W and JWST/NIRCam F115W, F150W, F187N, F200W, F300M, F335M, F405N, and F444W. In each filter, a detection lower than 3σ has been set as an upper limit. The results of the fitting process include sets of best-fitted values for eYSC and optical YSC physical properties (i.e., mass, age, and extinction), which are presented in the following section.

3.4. Final eYSC and Optical YSC Catalog in M83

Because eYSCs and optical YSCs have been extracted independently, we crossmatched the two populations for overlaps using a tolerance of a four-pixel (∼3.6 pc) radius. The sources that have entered the catalogs twice have been removed from the eYSCs and tagged as oYSCs. We find that less than 5% of systems in each eYSC class are in the oYSC catalog. We summarize in Table 1 the number of systems in each class. The final photometric catalogs refer to high-confidence level detected candidates in each class, after magnitude selections have been applied. The final number of candidates in each class includes objects with $\chi^2_{\rm red} < 20$ (the latter mild selection has been chosen after visual inspection of the fits to avoid inclusion of catastrophic fit failure) and uniquely identified in emission line maps or optical broadband colors. In the rest of this work, oYSCs refers to optically selected YSCs with ages lower than 10 Myr.

We present the identified eYSCs and oYSCs (inside FOV) populations in Figure 3. We note that the position of eYSCs coincides with the spiral arms and dust lanes highlighted by the optical colors, while oYSCs are mainly located in UV bright regions, adjacent to spurs and feathers created by the drifting of the spiral arms.

Final photometric catalogs and CIGALE SED fit outputs will be released at https://feast-survey.github.io.

4. Results

In this section, we explore the observed IR colors of the eYSCs and oYSCs and compare them to the inferred physical properties obtained with CIGALE SED fits.

4.1. Observed IR Colors of Emerging YSCs

We use color–color diagrams as diagnostic diagrams to analyze the cluster population in the galaxy. Color–color plots with UV-optical filters are used to study the properties of the YSCs (and oYSCs in particular), while JWST NIR colors are used to describe the observed color of eYSCs that can provide insights into their physical properties. We compare the location of the different cluster populations to two sets of integrated star cluster evolutionary models: Yggdrasil single stellar population (SPP) models (E. Zackrisson et al. 2011) and MAPPINGS III (B. Groves et al. 2008). The Yggdrasil evolutionary track is produced by assuming solar metallicity and sampling the cluster stellar population with a P. Kroupa (2001) IMF and redshifted to $z = 0.001711$. When relevant, at young ages, the Yggdrasil model includes nebular emission, assuming that 50% of the ionizing photons produced by the SSP ionize the gas in the nebula. On the other hand, the MAPPINGS III model assumes a compactness parameter $C = 10^5$, gas pressure $P_0/k = 10^5$ K cm^{-3}, H I column density $\log N(\mathrm{H\,I}) = 10^{21.5}$ cm^{-2}, and fraction of PDR, where $f_{\rm PDR} = 0$ (i.e., no PDR included, labeled MAPPINGS–H II) and $f_{\rm PDR} = 1$ (standard PDR model, labeled MAPPINGS-PDR +H II). The MAPPINGS model samples ages from 1 to 10 Myr, while Yggdrasil samples from 1 Myr to 14 Gyr. Model spectra are convolved with the filter responses.

On the top-left side of Figure 4, we show the $U-B$ (F336W −F438W) versus $V-I$ (F547M or F555W−F814W) colors of the optical YSC population. We show as filled dots the final YSC population (with $\chi^2_{\rm red} \leqslant 20$ and error lower than 0.2 mag; see Table 1) within the NIRCam footprint, color coded accordingly to their best-fitted ages from CIGALE. We also highlight the median color of the oYSCs younger than 10 Myr and with a secure detection in the NIRCam filters (photometric error less than 0.2 mag in F150W, F115W, F187N, F200W, F300M, F335M, and F444W). On average, the optical color of the oYSCs is close to the 5–10 Myr

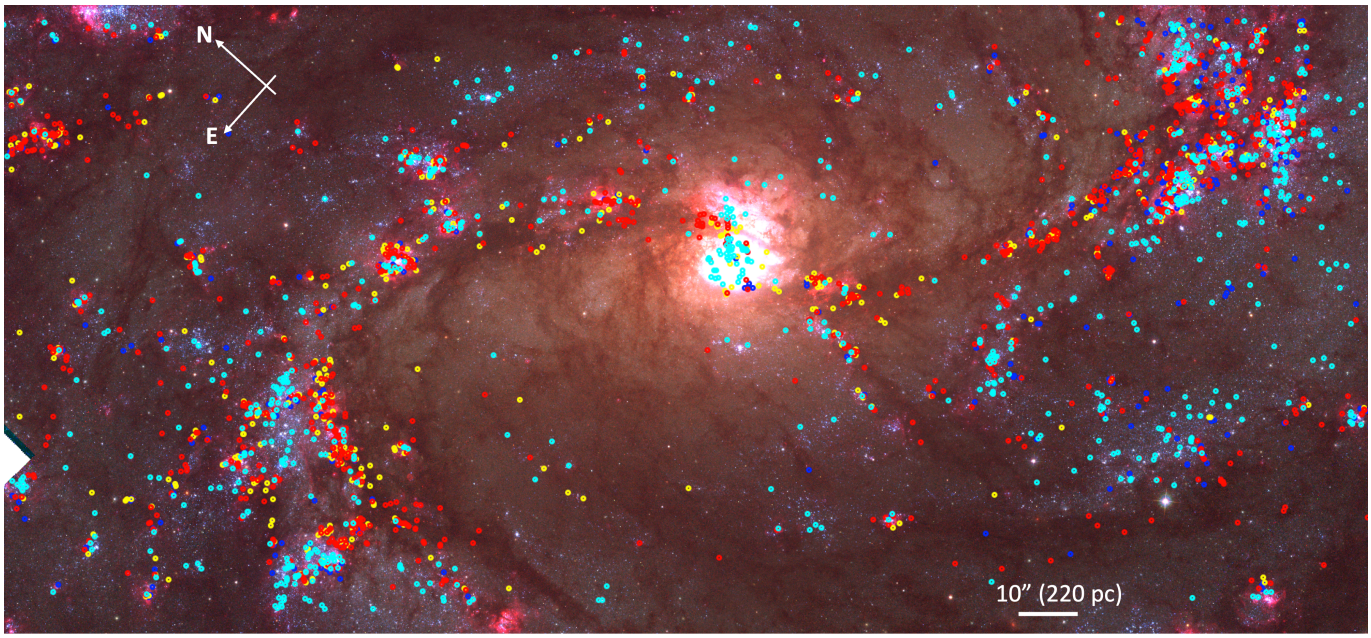

Figure 3. A three-color HST composite of the FEAST JWST FOV. The mosaic shows the HST/F336W (blue), HST/F438W (green), and HST/F657N (red) bands. Different populations of star clusters are overplotted as circles, with eYSCI in red, eYSCII in yellow, 3.3 μm PAH peaks in blue, and oYSCs (younger than 10 Myr) in cyan. We note that eYSCs are closely located along dusty lanes, while YSCs are cospatial with the regions with the strongest near-UV radiation.

parameter space of the Yggdrasil model. We stress that Yggdrasil and CIGALE use the same stellar libraries; thus, even if the ages are not derived with the model track used in the plot, their agreement is good (Linden et al. 2025, in preparation). In general, the star cluster population within the FOV is representative of the overall population within the disk, shown by the gray contour.

In the remaining panels of Figure 4, we focus on the IR colors of the eYSC populations. In the top-right plot, we look at the F150W−F200W versus the F200W−F335M. The *y*-axis color is sensitive to the stellar photosphere, and therefore to stellar evolution. The *x*-axis color includes the medium-band filter F335M, which is dominated by the 3.3 μm PAH band in the early stages. The MAPPINGS models that include treatment of this feature indeed show a large variation in the latter color during the early stages of cluster evolution. We also include a color excess arrow illustrating the direction of increased extinction, estimated with the Extinction Python package (K. Barbary 2017) assuming a J. A. Cardelli et al.'s (1989) extinction law and the gradient of the extinction curve at a visible wavelength, $R_V = 3.1$ (B. T. Draine 2010). S. T. Linden et al. (2023) used this color space to isolate the most embedded star clusters in massive starburst galaxies. Their proposed color selection, i.e., the top-right area enclosed by dashed lines, is based on the presence of extinction and excess emission in the 3.3 μm PAH band, and overlaps with the color distribution of the reddest eYSCs. By focusing on the median colors, we see a clear evolution sequence from eYSCI (red-orange triangles) to eYSCII (orange-yellow squares) and oYSCs (blue circles), suggesting the emergence of the star clusters and the rapid disappearance of the PDR. The eYSCII have on average weaker 3.3 μm PAH emission than eYSCI and 3.3 μm PAH peaks, in agreement with the lack of association with a compact/concentrated emission. After applying the color selection (S. T. Linden et al. 2023) to our catalog of eYSCs, we find that 319 (28.0%) eYSCI, 64 (14.0%) eYSCII, and 61 (15.0%) 3.3 μm PAH peaks occupy the upper-right corner area. These are the fractions of eYSCs that have comparable colors to the embedded star clusters as defined and selected by Linden and coauthors.

In the lower-left plot, we show another color combination. On the *y*-axis, we plot the F300M−F444W with the F300M still dominated by stellar emission. The wide-band F444W filter is dominated by several molecular and H-line emission lines as well as a hot dust component, especially strong in star-forming regions. The F300M−F335M is another indicator of the strength of the PAH band. On average, eYSCs spread again in an evolutionary sequence with the oYSCs sitting closest to the star cluster models when the F444W is included.

In the lower-right plot, we compare the F200W−F444W versus the F115W−F187N. The color used in the *y*-axis has been used (at similar wavelengths) in studies of YSOs in the Magellanic Clouds with JWST (N. Habel et al. 2024) and in the massive star-forming region Cygnus X with Spitzer (R. Pokhrel et al. 2020) and is sensitive to the hot dust. The *x*-axis color is sensitive to the Paα excess. On average, we see that eYSCs occupy the same color space of YSOs in galaxies in the Local Volume, shown by the dashed (F115W −F187N > 0 and F200W−F444W > −0.6; N. Habel et al. 2024) and dotted lines (F200W−F444W > −0.6; R. Pokhrel et al. 2020). Their average Paα emission is significantly stronger than in the oYSCs, even though the latter have still quite young ages. Overall, the behavior of the oYSCs is expected if their average ages are older than the eYSCs.

The picture conveyed by the NIR color analysis is that, with our emission-based extraction, we are able to detect recently formed star clusters in a broad range of emergence states. On average, the eYSCs are characterized by red 4 μm colors, and strong emission in hydrogen and 3.3 μm PAH emission. Their 4 μm colors fully overlap with YSOs observed within the Local Volume, suggesting that a significant fraction of their stars might not have yet reached the main sequence and are in the accretion phase. On the other hand, the oYSCs show a spread, and we clearly see that a fraction of the optically

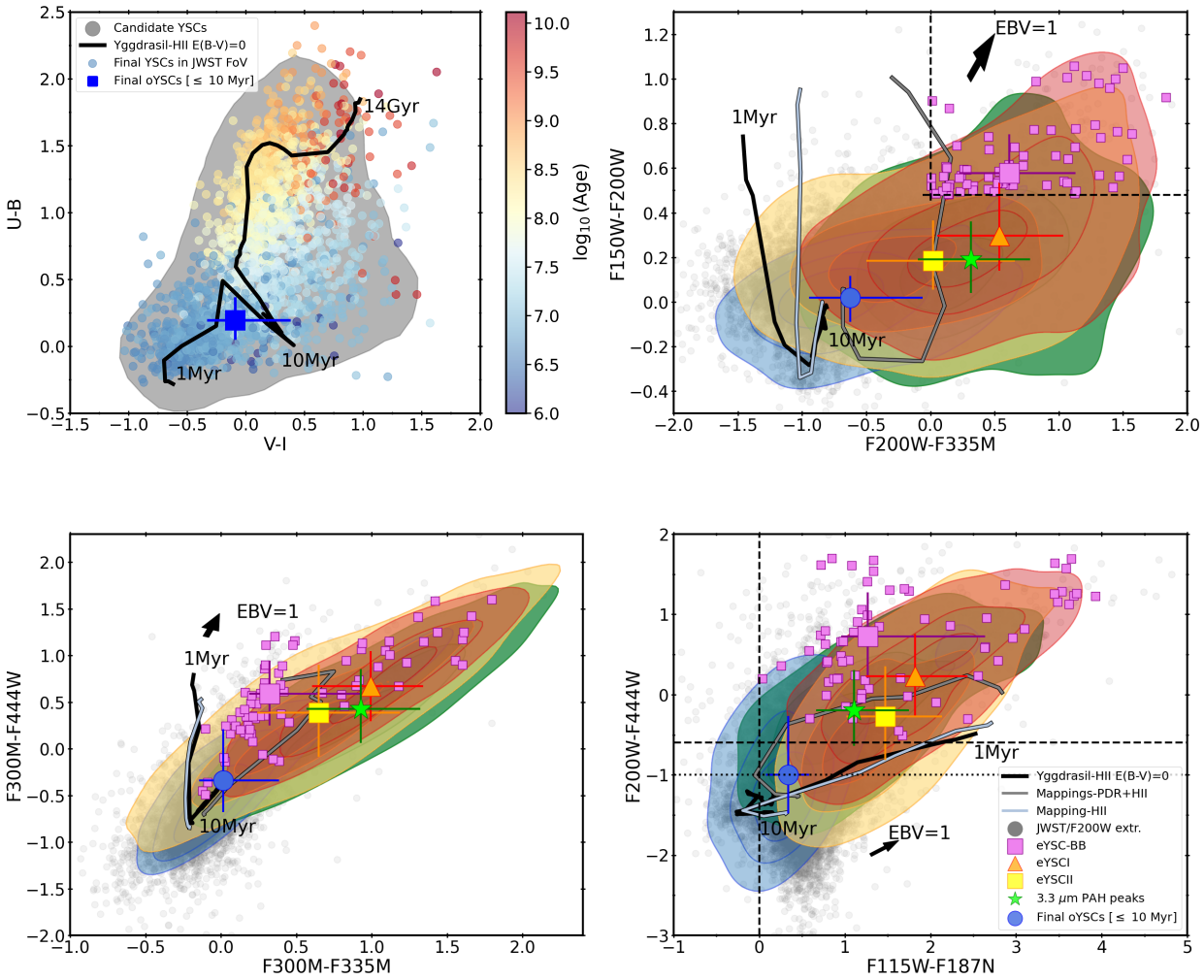

Figure 4. Top left: $U-B$ (F336W–F438W) against the $V-I$ (F547M or F555W−F814W) together with the Yggdrasil SPP model (black solid line). The gray distribution illustrates the entire optical YSC population after visual inspection, while the dots show all the YSCs within the FOV (see Table 1) color coded by the best-fitted ages. The blue square shows the median colors of oYSCs ($\leqslant$10 Myr) within the NIRCam FOV and photometric error less than 0.2 mag in F150W, F115W, F187N, F200W, F300M, F335M, and F444W. The NIR color–color diagrams in the upper-right, lower-left, and lower-right corners illustrate the eYSCI (red-orange triangles and red distributions), eYSCII (orange-yellow squares and yellow distributions), 3.3 μm PAH peaks (green stars and green distributions), F200W-extracted sources (gray circles), eYSC-BB (purple squares), oYSCs (as defined above, blue circle and blue distributions) together with the Yggdrasil SPP model (black solid lines), MAPPINGS III-H II (light-gray), and MAPPINGS III-PDR+H II models (dark-gray solid lines). Top right: the F150W−F200W against the F200W−F335M. The box displays the color–color selection for embedded clusters from S. T. Linden et al. (2023). Lower left: the F300M−F444W against the F300M−F335M color. Lower right: the F200W−F444W against the F115W−F187N color together with dashed and dotted lines to illustrate the color space of YSOs. The distributions are contours with levels at 16%, 50%, and 84% percentiles. The gray contour in the top-left plot shows the 95% percentile of the total cluster candidates after visual inspection.

detected clusters with ages less than 10 Myr overlap with the space occupied by eYSCs, but their NIR properties are less extreme, as already reported by M. Rodríguez et al. (2025) for other local galaxies.

4.2. Cluster Physical Properties from the SED-fitting Analysis

Next, we present the distributions of the physical properties derived from the SED-fitting analysis described in Section 3.3. We focus on eYSC and oYSC candidates that have solid detections and good $\chi^2_{\rm red}$ (see Table 1). For the oYSCs, we select only those within the NIRCam FOV. We will first describe the recovered trends in cluster ages, masses, and extinctions, and then discuss their reliability.

In Figure 5, we present the stellar age (left), color-reddening distributions (middle), and mass (right) of each eYSC class and oYSCs, separately. We show median values of ages and $E(B-V)$ for each class as vertical lines. We observe that the eYSCI and eYSCII are on average the youngest and most attenuated systems, followed by older and less attenuated oYSCs. The 3.3 μm PAH peaks are at face value the oldest population. We also notice that only a small fraction (5%) of the oYSCs have ages below 3 Myr, while we find that this fraction increases to 30% for eYSCI, 25% for eYSCII, and 16% 3.3 μm PAH peaks. In the right panel, we show the mass distributions for each eYSC class and the oYSCs. We include a power-law cluster mass function (CMF) with a slope of −2 (M. R. Krumholz et al. 2019) to guide the reader to the expected shape of this distribution in the diagram. The oYSCs have a larger number of massive star clusters above 10^4 $M_\odot$, and they are mainly associated with the central starburst region (see Section 5.3). The turnover of the eYSC mass around 10^3 $M_\odot$ is due to incompleteness. The peak appears at lower masses in the oYSC population. Both populations follow

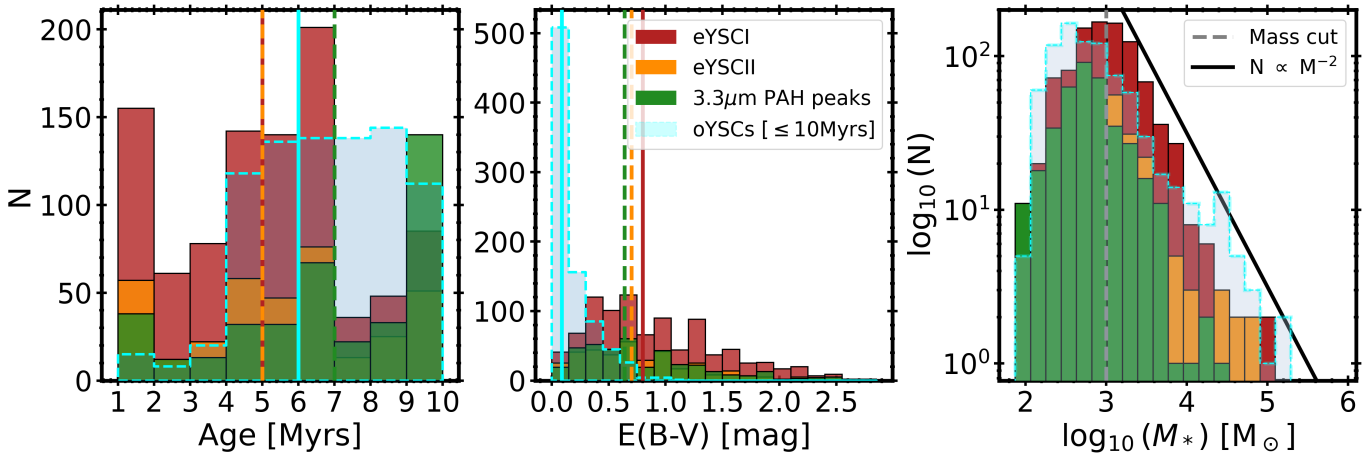

Figure 5. The stellar age (left), stellar attenuation (middle), and stellar mass distribution (right) for the different classes, eYSCI (red), eYSCII (orange), and 3.3 μm PAH peaks (green) including the oYSCs ($\leqslant$10 Myr; cyan) derived with CIGALE. The vertical lines correspond to the median values of eYSCI (red), eYSCII (orange), 3.3 μm PAH peaks (green), and the optical YSCs ($\leqslant$10 Myr; cyan). The mass distribution (right) also includes a gray dashed line corresponding to the mass cut at 10^3 $M_\odot$ and the black curve to the 10-logarithm of a cluster mass function (CMF) with a slope of -2. For the stellar age (left panel), the eYSCI median overlaps with the eYSCII.

the -2 power-law distribution, similarly reported by R. C. Levy et al. (2024) and S. T. Linden et al. (2024) for embedded star clusters. We find 48% of eYSCI, 39% of eYSCII, and 25% of the 3.3 μm PAH peaks are more massive than 10^3 $M_\odot$, while only 30% of the oYSCs have masses above this limit (illustrated by the gray vertical line in Figure 5).

We note that stochastic IMF sampling is definitively a limitation for the recovered values of cluster physical properties. It is well known that the use of deterministic models (e.g., Yggdrasil, CIGALE, MAPPINGS) when fitting star cluster SEDs leads to relatively biased physical properties, especially as a function of cluster mass (e.g., M. Cerviño & V. Luridiana 2004; M. Fouesneau & A. Lançon 2010; J. Maíz Apellániz 2010; M. R. Krumholz et al. 2015). Here, a large fraction of clusters in all categories have masses below 10^3 $M_\odot$, and thus we expect their ages to be unreliable due to stochastic IMF sampling. J. Maíz Apellániz (2010) tested the effect of stochasticity using as a baseline an SED with U-to-NIR broadband colors. They concluded that such an extended baseline is beneficial to recover a reliable cluster age, except in the red supergiant (RSG) phases around 10–30 Myr. M. Fouesneau et al. (2012) reached a similar conclusion using U to I bands, showing that RSG colors scatter the recovered ages of clusters, creating an artificial gap in the age distributions at 10–30 Myr and overpopulating the age range 6–10 Myr. With the addition of NIR broadband colors, M. Fouesneau & A. Lançon (2010) showed that even the asymptotic giant branch phases become critical for star cluster physical property recovery. These limitations are also inherited from the stellar evolutionary models that lack good prescriptions for these stellar phases.

Related to the age range explored in this work, we report some important considerations. Since we limit the analysis to the cluster populations within the overlap area of HST and JWST FOVs, all cluster candidates in the emerging as well optical categories potentially have UV-to-5 μm detection. Adamo et al. (2025, in preparation) and Pedrini et al. (2025, submitted) suggest that some of the IR colors of the oYSCs as well as eYSCs suffer indeed from stochastic sampling effects. These works, however, highlight that the inclusion of three H recombination lines in the SED analysis (Hα, Paα, and Brα) largely mitigate the age-extinction degeneracy that affects most of the broadband studies (e.g., D. Calzetti et al. 2015; B. C. Whitmore et al. 2020, although the latter only included Hα in their analysis). In particular, Pedrini et al. (2025, submitted) report a clear NIR excess in the eYSCs in the FEAST galaxies. This excess results in poor fits of the NIR continuum and overestimation of the eYSCs ages. Therefore, it is very likely that the true ages of the eYSCs are younger than reported by the SED analyses. The IR colors of eYSCs clearly show Paα excess with respect to the oYSCs, confirming that the latter population is older compared to the recovered ages from the SED analysis.

We speculate here that the difference in mass distributions between eYSCs and oYSCs might be due to uncertainties in the recovered ages but also to the dynamical properties of the environment probed by our observations and the limited area covered by the FOV. M83 is the only target among the FEAST galaxies featuring a strong bar. The JWST FOV encloses the bar, the end of the bar, and the circumnuclear starburst ring (see Figure 1). These are the dustier regions in M83 and the areas where recent star formation is more enhanced. In Figure C1 in Appendix C, we show the ages, $E(B-V)$, and masses of the oYSCs within the entire HST FOV. We see that the median age of the entire population becomes slightly younger (5 Myr instead of 6 Myr), the median $E(B-V)$ remains very low, and the mass distributions of the oYSCs peak at similar low masses as observed within the JWST FOV. However, we recover masses that are more similar to those observed in the eYSC populations. It is possible that rapid disk rotation and limited FOV causes a selection bias against the optical YSC populations. The difference in mass between eYSCs and YSCs might also be due to mass loss on short timescales because a large fraction of eYSCs are probably expanding stellar associations. We discuss these possibilities in the next section.

5. Discussion

In this study, we present the population of star clusters younger than 10 Myr in the star-forming galaxy M83. We extract the eYSC candidates in H recombination emission line

maps, Paα and Brα, and a 3.3 μm PAH emission map tracing the ambient H II region and PDR, respectively. The YSCs are detected in the optical using the F555W and F547M HST filters. We perform multiwavelength photometry from the UV to 5 μm using the `FEAST-pipeline` and derive their physical properties using the SED-fitting code `CIGALE`. The result is 1307 eYSCs, 389 3.3 μm PAH peaks, and 829 oYSCs residing within the JWST NIRCam FOV.

5.1. The 3.3 μm PAH Peaks

In Section 4, we presented the colors and physical properties derived for the 3.3 μm PAH peaks, identified as compact emission sources in 3.3 μm PAH emission but not significantly in H recombination lines. The colors of the 3.3 μm PAH peaks (Figure 4) can be explained by strong emission in the PAH band, while, compared to the eYSCs, they have on average the lowest emission in Paα. Their colors are also different from the eYSC-BB, suggesting that these are not (only) deeply embedded clusters. Focusing on CIGALE SED outputs (Figure 5), we see that, in general, this class is associated with older ages and similar attenuation but lower masses than eYSCI. The lack of a compact/strong H II region associated with these systems might lead deterministic models to age date these systems as older on average. We speculate here that these systems might be those clusters that do not host stars massive enough (detection limit corresponds to a 15 $M_{\odot}$ or O9.5V spectral type) to power a detectable H II region. PAH molecules are excited by nonionizing UV radiation and for a population of B stars could still result in detectable PAH emission. Both explanations, older systems or young but not hosting massive stars, could explain this population. Due to their uncertain nature, we have reported their detection and derived physical properties, but we will not include them among the eYSCs in the following discussion.

5.2. Are All eYSCs Gravitationally Bound?

A stellar cluster, as mentioned in the introduction, can be gravitationally bound or unbound. For example, the YSCs classified according to the LEGUS scheme (A. Adamo et al. 2017) as classes 1 and 2 have higher probability of being gravitationally bound, while class 3 are more likely stellar associations. This morphological classification has been based on the measurements of the dynamical age, defined as the ratio between the cluster age and its crossing time (M. Gieles & S. F. Portegies Zwart 2011; J. E. Ryon et al. 2017; G. Brown & O. Y. Gnedin 2021). However, this method does not work on star clusters that are too young, since the crossing time becomes comparable to the stellar age (M. Gieles & S. F. Portegies Zwart 2011). Star formation is clustered in nature, which challenges our understanding of the formation of gravitationally bound star clusters with respect to stellar associations. Initial numerical simulations suggested that the formation of a stellar association was the result of an expanded bound cluster, unbounded by rapid gas dispersion (e.g., P. Kroupa 2001; S. P. Goodwin & N. Bastian 2006). The implications of these works are that the majority of star formation would take place in bound clusters. However, more realistic initial conditions for a GMC collapse can, even at the start, produce stellar associations (e.g., R. J. Parker et al. 2014; C. L. Dobbs et al. 2022; M. Y. Grudić et al. 2022). Some recent observational studies (e.g., M. Kounkel et al. 2018; J. L. Ward et al. 2020) also suggest that expanding associations are initially more compact but still unbound. This is further supported by the fact that a large majority of young systems, i.e., embedded clusters, are actively expanding (M. A. Kuhn et al. 2019).

In this work, we can use eYSC and oYSC relative numbers as an indication of what fraction of eYSCs we should expect to be potentially bound. While we cannot yet establish the eYSC boundness using, for example, their dynamical age, we can compare total numbers of eYSCs and oYSCs to derive a first-order estimate of the fraction of bound clusters within the eYSCs. In this exercise, we assume that the galaxy star formation rate (SFR) is constant within 10 Myr, that eYSCs are precursors of oYSCs, and associations dissolve within 10 Myr, which is reasonable since we look at compact systems within a few parsec scales. Among the oYSCs younger than 10 Myr, we have classified ∼36% (299 oYSCs) as likely bound (class 1 and 2), while the remaining 64% are short-lived associations (530 systems as class 3). If we compare the number of bound oYSCs with the total number of eYSCs (eYSCI+eYSCII), we find that N(YSCs (class 1 and 2))/N (eYSCI+eYSCII) ∼23%. If we apply a mass cut of 1000 $M_{\odot}$, the fraction goes down to 16%. In other words, only about 20% of the eYSCs could potentially be bound while the majority are likely associations. This result agrees with observations in the Milky Way (C. J. Lada & E. A. Lada 2003), where most of the stellar associations dissolve within 10 Myr, as well as numerical works such as J. P. Farias et al. (2023), who found that most of the star clusters formed in the STARFORGE simulations are unbound.

5.3. Physical Properties of eYSCs and YSCs as a Function of Galactic Environments

Previous studies of the YSC (N. Bastian et al. 2012; A. Adamo et al. 2015) and GMC (P. Freeman et al. 2017) populations of M83 find that their mass distributions can be described by a power law with a slope of −2, while the upper-mass end is consistent with an exponential cutoff mass that changes in different galactic environments. These studies pointed out that the nuclear starburst and the end of the bar regions appear to be more efficient in forming more massive clusters, in agreement with analytical and numerical model predictions (M. Reina-Campos & J. M. D. Kruijssen 2017; A. A. Ali et al. 2023).

The eYSC population detected in this work is the connecting step between oYSCs and GMCs. We therefore investigate here whether the mass distributions of the eYSCs show consistent variations. First, we divide the FOV in radial annuli as a function of distance from the center in an informed way. Each annulus contains a specific environment (see Figure 1): the center within 0.34 kpc, the bar between 0.34 and $R_g < 2.1$ kpc, the end of the bar connecting with the spiral arm at $2.1 \leqslant R_g < 3.3$ kpc, and the outer regions. Since we are focusing on stellar populations formed within 10 Myr, we expect that each annulus contains systems formed under the same physical conditions. The number of eYSCs and oYSCs in each region are reported in Table 2.

In Figure 6, we show the age (bottom) and mass (top) distributions of the combined eYSCs (left) and of the oYSCs (right) for each informed environment. Overall, the median ages of the eYSCs and YSCs in the different environments coincide with those seen in the respective populations in

Table 2
The Emerging and eYSCI Timescale for the Different Galactic Environments Presented in Figure 1, together with the Galactocentric Distances Enclosing the Region and the Number of eYSCI, eYSCII, and oYSCs in Each Environment

Sample M ($M_\odot$) or R_g (kpc)	eYSCI → oYSC (Myr)	eYSCI → eYSCII (Myr)	eYSC I+II, oYSC #
Whole galaxy	6.1 ± 0.1	4.4 ± 0.1	946+361, 829
Low mass (1e3 $< M \leqslant$ 5e3)	7.4 ± 0.2	5.7 ± 0.2	394+121, 181
High mass($M >$ 5e3)	5.3 ± 0.4	4.0 ± 0.4	56+19, 66
Informed environmental division			
Center [$R_g < 0.34$]	4.0 ± 0.5	2.4 ± 0.5	22+14, 55
Bar [$0.34 > R_g \leqslant 2.1$]	6.5 ± 0.2	4.3 ± 0.2	256+128, 207
End of the bar [$2.1 < R_g \leqslant 3.3$]	6.1 ± 0.1	4.6 ± 0.1	521+168, 449
Outer regions [$R_g > 3.3$]	6.3 ± 0.3	4.7 ± 0.3	147+51, 118
Regions containing the same number of eYSCs+oYSCs			
Bar [$0.34 < R_g \leqslant 1.9$]	6.3 ± 0.2	4.2 ± 0.2	214+108 , 189
Leading end of the bar [$1.9 < R_g \leqslant 2.5$]	7.1 ± 0.2	5.2 ± 0.2	276+96, 148
Trailing end of the bar [$2.6 < R_g \leqslant 2.9$]	5.6 ± 0.2	4.2 ± 0.2	212+74 , 225
Outer region [$R_g > 3.0$]	5.9 ± 0.2	4.5 ± 0.2	231+69, 212

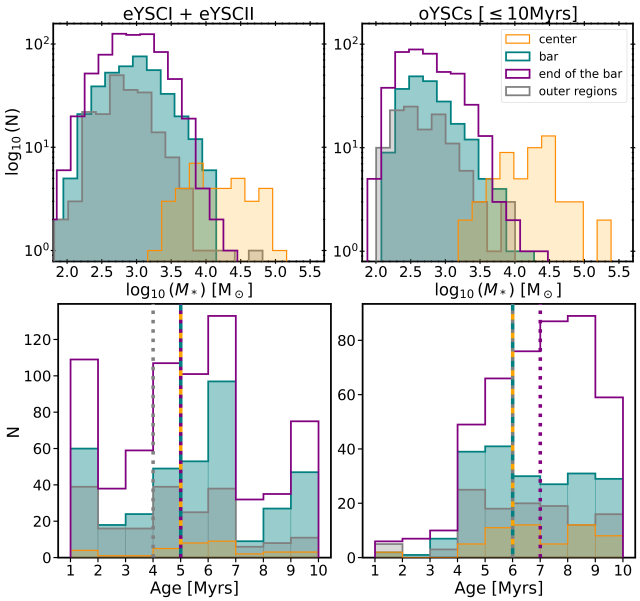

Figure 6. The mass (top) and age (bottom) distributions of the combined eYSCI and eYSCII sample (left) and oYSCs (right) as a function of different galactic environments selected to encompass different dynamical regions of the galaxy: center (yellow); bar (teal); end of the bar (purple); outer regions (gray). The turnover in the mass distributions is due to incompleteness. The vertical lines in the bottom plot show the median ages in each region.

Figure 5, with the exception of eYSCs in the outer regions appearing slightly younger and the oYSCs at the end of the bar annulus being slightly older than average. In the top plots, the flattening and turnover of the distributions show at which mass incompleteness becomes severe. The center, bar, and the end of the bar are the most affected, while the outer regions have lower mass incompleteness. The eYSC and oYSC mass distributions in the center stand out with respect to the rest of the disk. While incompleteness is severe, we also see that this region is the one where the most massive clusters are currently forming, confirming previous results in this galaxy (e.g., J. Harris et al. 2001) and in nuclear starburst rings in general (e.g., T. P. R. van der Laan et al. 2015). The bar and end of the bar region contains the largest number of eYSCs and oYSCs and sample clusters up to a few 10^4 $M_\odot$. The outer regions contain a modest number and have the least massive clusters. A Kolmogorov–Smirnov test using `scipy.stat.kstest` produces p-values below 0.05 for the null hypothesis that the mass distribution of oYSCs (eYSCs) in the (end of) bar versus outer regions are drawn from the same distributions. These observed trends are very similar to that reported by A. A. Ali et al. (2023), who simulated star cluster formation in clouds extracted in diverse galactic environments. They also found that clusters forming in molecular clouds affected by bar potential are able to sample more massive star clusters than in the spiral arm and interarm region.

We try next to assess whether the dynamical features in the disk of the galaxy (e.g., bar, spiral arm, interarm) organize cluster formation in the same way they organize star formation. We divide the galaxy disk area outside of the center in annuli containing the same number of eYSCs +oYSCs (see the blue circles in Figure 1). Assuming that cluster formation is a constant fraction of the SFR in the last 10 Myr, dividing the regions based on the same number of clusters should overcome SFR variations. Overall, this division produces annuli covering the bar and the outer region in a similar fashion as before, but it divides the end of the bar region into two; we refer to these new annuli as the leading (closer to the bar) and trailing (closer to the spiral arm) end of the bar. In Figure 7, we plot the mass and age distributions in these alternative annuli. The mass distributions of the eYSCs in the bar and leading end of the bar annuli have more massive clusters than the trailing and outer region annuli (with some exceptions for the latter). These differences are not as clear in the mass distributions of the YSCs. Interestingly, when looking at the age distributions in Figure 6, we see that the median age distribution of the eYSCs does not change with respect to the previous division. On the other hand, the division of the bar highlights that the average older population seen in the oYSCs (bottom-right panel of Figure 6) is preferentially associated with the trailing side of the bar connecting with the spiral arm, likely due to strong dynamical drifting associated with that region.

We conclude here that, while the center stands out for its ability to form very massive star clusters, the differences seen

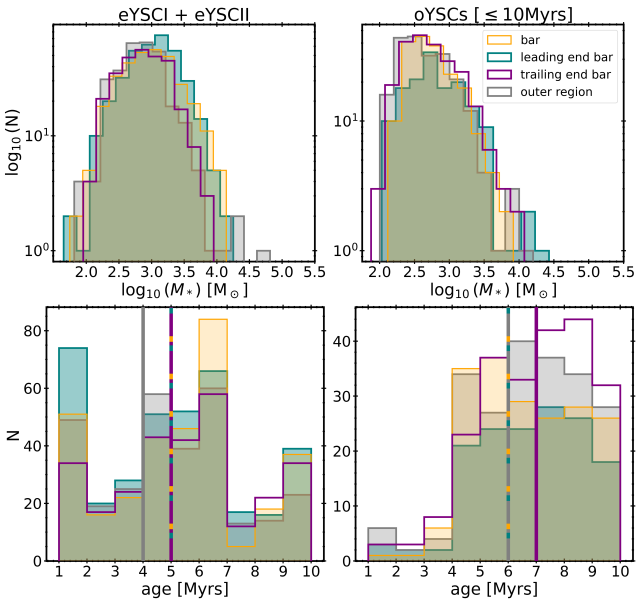

Figure 7. The mass (top) and age (bottom) distributions of the combined eYSCI and eYSCII sample (left) and oYSCs (right) in bins containing the same number of eYSCs and oYSCs combined. The central starburst region has been removed. This alternative division is less sensitive to changes in SFR due to different dynamical properties. The turnover in the mass distributions is due to incompleteness. The vertical lines in the bottom plot show the median ages in each region.

in the eYSC and YSC mass distributions in the disks are likely driven by the increase in SFR. The latter results in a sampling of the mass function to higher masses. This result is in agreement with recent analyses of molecular clouds in local spiral galaxies (e.g., J. Sun et al. 2020; M. Querejeta et al. 2024; H. Faustino Vieira et al. 2025) that find noticeable differences between the molecular cloud properties in the center of the galaxies, while these differences become smaller in the disk, i.e., the spiral arms appear to organize star formation but not enhance it. We also notice that the limited coverage reduces the sampling of the disk environment, especially the arm and interarm regions, and therefore our conclusions might be biased by limited statistics. In a follow-up work, we will provide an in-depth analysis of the eYSCs and YSCs population across the FEAST galaxies to test environmental dependencies on the shape of the mass function.

5.4. The Emerging Sequence of Star Clusters

One of the main goals of this study was to estimate the emerging timescale, that is, the time it takes for an eYSC to disperse its natal cloud. These timescales are fundamental to set the integrated star formation efficiency in the GMCs where star clusters are forming as well as the timescales for stellar feedback to disrupt the natal GMC.

In Section 4, we found that eYSCI and eYSCII are younger and more attenuated than the oYSCs. In Figure 4 (upper right), we see evidence that the eYSCs follow an evolutionary track, with the eYSCII located at bluer IR colors and, therefore, being the least embedded, followed by the 3.3 μm PAH peaks and, lastly, the eYSCI at a redder color, being the most embedded star clusters detected in this study.

Using a broadband color selection aimed to find the most embedded star clusters not necessarily associated with Paα emission resulted in the extraction of only 70 eYSC-BB not yet classified as eYSCs (about 5%). This small fraction, similar to what is found in NGC 628 (Adamo et al. 2025, in preparation), would suggest that the deeply embedded phase, prior to the massive stars reaching the main sequence and starting to power detectable H II regions, is significantly shorter when compared to the phase dominated by ionized gas emission. The 3.3 μm PAH peaks could potentially contain deeply embedded clusters or clusters that did not form massive stars. However, we see that only 15% of this class has colors compatible with this selection, reinforcing the conclusion that the deeply embedded phase is short when compared to the other phases. This evidence is in agreement with high-spatial resolution studies of embedded cores conducted in the Milky Way (N. J. Evans et al. 2009; A. Duarte-Cabral et al. 2013), where the accreting protostellar phase (i.e., corresponding to Class 0/I YSOs) appears to be very short ($<$1 Myr).

The evolutionary sequence identified here is mainly based on the PAH emission feature prominence between classes, where the eYSCI have a compact and stronger PAH emission (brighter F335M magnitude) than eYSCII. This difference would imply an evolution in the morphology of the PDR associated with the 3.3 μm PAH emission. A. Pedrini et al. (2024) find evidence that supports this hypothesis by reporting differences between the PDR morphology for classes of eYSCs and, especially, a decrease in the 3.3 μm PAH emission feature with cluster age. In conclusion, the physical properties of eYSCI, eYSCII, and oYSCs argue for a complete sampling of the evolutionary sequence from deeply embedded to exposed. As discussed in Adamo et al. (2025, in preparation), studies based on JWST broadband color selections and the excess of 3.3 μm PAH emission (S. T. Linden et al. 2023, 2024; M. J. Rodríguez et al. 2023; B. C. Whitmore et al. 2023; R. C. Levy et al. 2024; M. Rodríguez et al. 2025) are sensitive to the embedded phase, e.g., traced here by the eYSCI class, but miss the eYSCII class. Pre-JWST studies based on the intensity of H recombination lines (K. Hollyhead et al. 2015; S. Hannon et al. 2019, 2022; M. Messa et al. 2021; S. Deshmukh et al. 2024; T. McQuaid et al. 2024; e.g., Hα, Paβ) miss a significant fraction of embedded objects (eYSCI) due to progressively higher extinction, but also due to the lower resolution of previous NIR studies, which are now revealed by the more sensitive JWST data as well as sampling up to 5 μm. Incomplete sampling of either of these evolutionary phases leads to shorter timescales. We therefore use the emerging YSCs in M83 to derive a more reliable timescale than previous studies.

5.5. Cluster Physical Properties along the Emerging Sequence

Combining HST narrowband Paβ with UV-optical broadband imaging, M. Messa et al. (2021), S. Deshmukh et al. (2024), and T. McQuaid et al. (2024) reported a weak anticorrelation between age and extinction, with a significant fraction of clusters associated with Paβ emission having only moderate extinction already from early ages. In NGC 4449, T. McQuaid et al. (2024) found that more massive clusters are associated with lower attenuation, suggesting that the clearing timescales could be shorter for more massive clusters. Following these previous analyses, we plot the age and mass distributions of eYSCs and oYSCs (left), the total visual extinction against the cluster mass (center), and the stellar age (right) in Figure 8. The left plot shows similar trends as seen in Figure 5, with eYSCs dominating the youngest age bins while

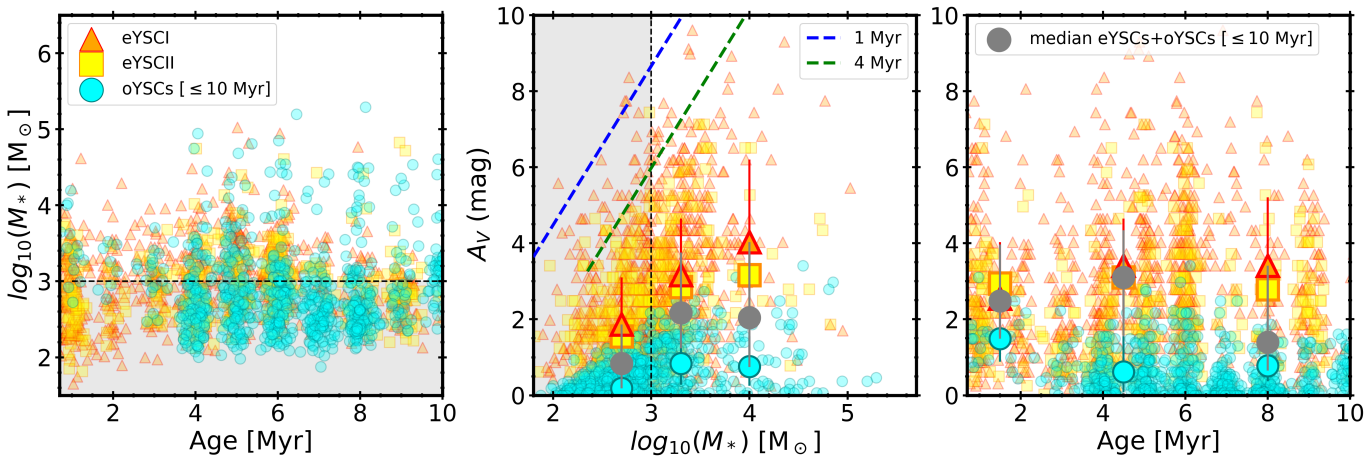

Figure 8. Physical properties of the combined cluster sample younger than 10 Myr. On the left, we show the age–mass distributions. The total visual extinction (A_V) is plotted against the stellar mass (middle) and age (right). We can observe the eYSCI (orange triangles), eYSCII (yellow squares), and YSCs ($\leqslant$ 10 Myr; blue circles). Large symbols show the median A_V for the eYSCI, eYSCII, and YSCs ($\leqslant$ 10 Myr) separately and combined (gray dots). In the middle plot, we use 10^3–5×10^3 and $> 5 \times 10^3$ $M_\odot$ mass bins to estimate median A_V. The dashed lines correspond to the detection limits for the maximum A_V as a function of stellar mass for star clusters with an age of 1 Myr (blue) and 4 Myr (green) estimated using Yggdrasil models. In the right plot, we estimate the median A_V in age bins 1–3, 3–6, and 6–10 Myr after the mass cut, to mitigate the effect of stochastic sampling in the age derivation. The gray areas highlight star clusters with mass below 1000 $M_\odot$.

the opposite is true for the oYSCs. The gray area highlights clusters with masses below 1000 $M_\odot$ where stochastic IMF effects will dominate. In the central and right panel, we plot A_V, estimated using the stellar extinction, $E(B-V)$, outputted by CIGALE, and the gradient of the extinction curve at a visible wavelength, $R_V = 3.1$ (B. T. Draine 2010). In the central panel, we include median and quartiles of A_V as a function of mass ($\leqslant 10^3$, 10^3–5×10^3, $>5 \times 10^3$ $M_\odot$) bins for each eYSC class and oYSCs as well their combined values (gray dots). We also show, as guidance, the detection limits for the maximum A_V as a function of cluster mass, assuming two representative age values estimated using Paα detection limits and Yggdrasil's models, to indicate how incompleteness affects the distributions. In all classes, low-mass clusters will be affected more by incompleteness at increasing values of A_V than massive ones. Although we include one bin below 1000 $M_\odot$ (gray region), it is important to remember that that bin is the one most affected by incompleteness and uncertainties due to stochastic IMF sampling. By focusing on median trends of A_V in the two mass bins above 1000 $M_\odot$, we do not see a clear correlation between mass and extinction in oYSCs. The eYSCs show a large scatter in A_V as a function of mass and a tentative positive correlation, i.e., that more massive clusters might be more attenuated. However, when combining the NIR and optical populations (gray dots), and also taking into account the incompleteness, we conclude that there is no evidence of a strong trend. We do not find a clear signal that clearing timescales might depend on cluster mass. This result might be driven by the uncertainties and biases in the recovered cluster physical properties or might be due to the assumption of a simple screen attenuation, which might not truly reflect the true dust geometry.

We finally focus on the A_V as a function of age in the right panel of Figure 8. We include median estimates of A_V as a function of three age bins (1–3, 3–6, and 6–10 Myr) using only clusters more massive than 10^3 $M_\odot$ to mitigate strong deviations by stochastic effects. We do not observe a clear trend for the eYSCs: the attenuation with age is consistent within dispersions. On the other hand, the optical counterpart of the YSCs has moderate attenuation during the first few megayears, which declines to almost zero. When we combine the two populations, we see a clear declining trend. At face value, the different behavior between the two populations could indicate orientation and projection effects at play. The first age bin is dominated by eYSCs and only a smaller fraction of YSCs. We see here that the clusters are associated on average (gray dots) with $A_V \sim 3$ mag. Only after 4 Myr does the attenuation decrease to $A_V \sim 1$ mag in the last age bin, suggesting clearing timescales of 5–6 Myr. In the last age bin (age $\geqslant$ 6 Myr), occupied by about 20% of the entire eYSC population, eYSCs have median $A_V \sim 3$ mag (yellow square and orange triangle). In Pedrini et al. (2025, submitted), we report that these apparently older and reddened eYSCs are not correctly fitted by CIGALE. This subgroup of eYSCs have strong Paα and Hα associated with them. Their Paα EW estimates suggest that they are younger than 5 Myr (Pedrini et al. 2025, submitted). Taking into account these uncertainties, the trend presented above becomes stronger: newly formed clusters go through an emerging phase initially associated with higher attenuation along the line of sight, which declines at older ages. The large scatter might be due to degeneracies between orientation effects as well as to uncertainties to where exactly attenuation is taking place along the line of sight. A similar trend in attenuation has also been reported for larger star-forming regions in NGC 628 by A. Pedrini et al. (2024), where the classification was based on PAH morphology.

5.6. The Emerging Timescales

Another way to derive emerging timescales is to not rely on inferred physical properties for the eYSCs but to look at the number fractions of star clusters in different emerging stages (e.g., B. C. Whitmore et al. 2023). For this exercise, we use as a baseline 10 Myr, since that is the assumed age limit to fit eYSCs (Section 3.3) and to select oYSCs. We use the number of eYSCI, eYSCII, and oYSCs reported in Table 1; for the oYSCs, we select only systems within the JWST NIRCam

FOV. The timescale is given as

$$t = \frac{N(\mathrm{eYSCI})+N(\mathrm{eYSCII})}{N(\mathrm{eYSCI})+N(\mathrm{eYSCII})+N(\mathrm{oYSCs})} \cdot \mathrm{age}, \quad (1)$$

where $N(X)$ corresponds to the number of X-type clusters, eYSCI, eYSCII, or oYSCs, and the age parameter is 10 Myr. This method makes two implicit assumptions: (1) the SFR is constant over the period considered; and (2) no cluster disrupts during this time interval. The total emerging timescale corresponds to the time period for the eYSCI and eYSCII to become YSCs. We also estimate in a similar way the length of the eYSCI phase by dividing only the number of objects in this phase by the total number of clusters.

The recovered timescales are reported in Table 2 for the galaxy region sampled by JWST and the different galactic environments introduced in Section 5.3. They should be considered as an upper limit to the real values as we expect that the oYSCs have been affected by some disruption. The errors are estimated using Poisson statistics and error propagation for the number of clusters. Unless specified, we do not apply any mass selection above 1000 $M_{\odot}$. By selecting only eYSCs and oYSCs more massive than 1000 $M_{\odot}$, we recovered timescales and trends consistent with those reported in Table 2. The emerging timescale for the covered portion of the galaxy is 6.1 ± 0.1 Myr. This is on average the time it takes a star cluster to go from embedded to fully exposed in M83. These timescales are similar to the ones derived above by comparing A_V versus age. They are longer than reported by K. Hollyhead et al. (2015) in M83, where using Hα morphology combined with cluster age they find that the clusters have dispersed their natal cloud by 4–5 Myr. The slightly longer timescales can be understood here by the more complete sampling of the emerging phase accessible with JWST.

The first phase, from embedded to not being associated with a compact PDR, e.g., the eYSCI phase, lasts about 4.4 ± 0.1 Myr. This timescale is comparable to those reported in the PHANGS galaxies (M. J. Rodríguez et al. 2023; B. C. Whitmore et al. 2023; M. Rodríguez et al. 2025) and the GOALS starbursts (S. T. Linden et al. 2023, 2024) where the 3.3 μm PAH emission has been used as a tracer.

Once a compact PDR is disrupted, it takes only about 2 Myr for an average cluster to not be associated with a compact H II region, e.g., the eYSCII phase. The short time spent in the eYSCII phase can explain the similar age distributions for the eYSCI and eYSCII (see Figure 5, left). These short timescales are similar to those reported in M83 by K. Hollyhead et al. (2015). The latter find that a cluster takes about 2 Myr to go from partially embedded to exposed phases. S. Deshmukh et al. (2024) recovered an emerging timescale of 2–3 Myr for Paβ identified clusters, similar to what we find for eYSCII.

Studies where molecular gas tracers are combined with mid-IR and UV-optical wavelengths recover timescales consistent with what we find here (e.g., E. Corbelli et al. 2017; K. Grasha et al. 2018, 2019; J. Kim et al. 2023). In particular, J. Sun et al. (2024), using high-spatial resolution observations with ALMA, HST, and JWST in the center of NGC 3351, report a starless phase lasting 1–2 Myr and a total time for the emergence sequence of 4–6 Myr.

In Table 2, we also report the timescales dividing the sample in mass bins. We overcome incompleteness and stochastic IMF sampling issues by looking at clusters between 1 and 5×10^3 $M_{\odot}$, which provide characteristic timescales for the average star cluster of a few $>10^3$ $M_{\odot}$ and for clusters more massive than 5×10^3 $M_{\odot}$ to provide representative timescales for $\sim 10^4$ $M_{\odot}$ clusters. We find that, in general, for low-mass clusters, the complete emergence timescales goes up to 7 Myr, while for the massive clusters it goes down to 5 Myr. We argue that this result is not in tension with the lack of a strong trend between A_V versus cluster mass in Figure 8 because orientation effects and the simplistic assumption of a dust screen geometry might affect any correlation there.

When focusing on different galactic environments, we notice that the overall emerging timescales are comparable except in the center of the galaxy (see Table 2). When using binning of equal numbers of combined eYSCs+YSC, we see that the emergence timescales go up to 7 Myr in the leading side of the end of the bar region. This region is dominated by eYSCs, while the trailing portion of the end of the bar, the one connected to the spiral arm, shows the opposite trend. As already mentioned above, strong drifting coinciding with this region probably drives the differences in the timescales; the latter reflects dynamical environmental effects more than average timescales.

The center of M83 stands out with respect to the rest of the galaxy disk for its elevated star formation activity and the presence of a large fraction of the massive star clusters in the sample. The SFR in the center is significantly higher than in the disk (e.g., A. Adamo et al. 2015). D. Callanan et al. (2021), combining detection of star clusters in different tracers, propose that the SFR in the center has a variability timescale shorter than 10 Myr due to the dynamics of the bar supplying gas toward the nuclear ring. They estimate that the last peak event occurred 5–7 Myr ago, producing the massive YSCs we observe today, while the region is currently in a lower star formation mode. We indeed find that, in the central region, the number of oYSCs is larger than the detected eYSCs. However, we notice that this observational trend can also be explained if the emerging phase of these massive eYSCs is faster, leading to a larger number of oYSCs versus eYSCs.

We will investigate the mass dependence of the star cluster emergence phase with stronger statistics by combining the YSC and eYSC populations for all the FEAST galaxies in an upcoming work (Pedrini et al. 2025, in preparation).

In the next section, we will discuss the emergence phase by comparing these results to observational and numerical results in the literature.

5.7. What Stellar Feedback Drives the Emerging Phase of Star Clusters?

Our analysis of the M83 cluster population suggests average emergence timescales of 6–7 Myr for typical cluster masses of a few thousand solar masses. We see initial evidence that the emergence timescales are shorter ($\sim$5 Myr) for clusters above 5000 $M_{\odot}$. These average timescales do not include the deeply embedded phases of clusters where protostars are still accreting. However, as seen in the Milky Way infrared dark clouds, this phase is very short ($<$ 1Myr; e.g., N. J. Evans et al. 2009).

Simulations of molecular clouds might help here to shed light on the dominant mechanism leading to cluster formation and feedback. Unfortunately, we do not have direct observational information of the physical properties of the molecular clouds that lead to the formation of the star clusters in M83, but we refer to the cluster mass end products to compare observations with simulations. The initial conditions of the molecular cloud, especially the density, have a large impact on

the resulting cluster mass and net star formation efficiency. The latter quantity and the type of stellar feedback are tightly intertwined and will determine the emergence timescale (cloud disruption in simulations) and whether clusters form bound as an end product (e.g., J.-G. Kim et al. 2018; M. Y. Grudić et al. 2021; H. Fukushima & H. Yajima 2022). In recent work by B. Polak et al. (2024), the authors find that denser/more massive clouds lead to the formation of more massive star clusters. Star formation efficiency is higher since radiative feedback and stellar winds remain inefficient to prevent the collapse. Their formation is also faster and their emergence timescales shorter. Similar results are obtained by J.-G. Kim et al. (2018), H. Fukushima & H. Yajima (2022), and S. H. Menon et al. (2023), among many others.

It is also important to compare the role that pre-supernovae (SN) versus SN feedback plays in shaping the cluster properties and leading to the disruption of the natal molecular cloud.

Assuming a very short, deeply embedded phase, emergence timescales of 5–7 Myr might imply that SNe feedback is necessary to clear the leftover material from the natal cloud, since SNe explosions are assumed to start at 4 Myr in spectral synthesis models (e.g., STARBURST99; C. Leitherer et al. 2014). However, the boundary mass for stars to explode as SNe is not yet well understood (H. T. Janka 2025). Moreover, since massive stars in star clusters are those dominated most by stochastic IMF sampling, the latter needs to be taken into account for the majority of the eYSC population in M83. M. Chevance et al. (2022) show that SNe explosions are significantly delayed for low-mass clusters ($<10^4$ $M_{\odot}$). In the meantime, stellar feedback in the form of photoionization, radiation pressure, and stellar winds shape the star formation efficiency in the cloud, the IMF, and the boundness of stars as well as the driving of H II region expansion (A. A. Ali et al. 2022; S. C. Lewis et al. 2023; S. H. Menon et al. 2023; E. P. Andersson et al. 2024). This is in agreement with H II region studies conducted in M83 by L. Della Bruna et al. (2022), and, in general, in local spiral galaxies (A. T. Barnes et al. 2021; A. F. McLeod et al. 2021; D. Pathak et al. 2025). When SNe explode, they will find an already processed medium and can therefore create large bubbles and clear the leftover gas of the natal clouds (e.g., for simulations see M. Y. Grudić et al. 2022; E. P. Andersson et al. 2024; for observations, see M. Sirressi et al. 2024). The shorter timescales we observe in more massive clusters might be due to the likelihood of these clusters hosting more massive stars and thus experiencing SNe feedback on shorter timescales.

The emerging timescales reported in this work do not reflect the lifetime or destruction of the natal cloud. However, the timescales over which we see the PAH emission associated with clusters disappear (3–4 Myr), in agreement with many other works in the literature, indicate that pre-SN feedback is the main driver of PAH disruption in star-forming regions. Due to the complex nature of PAH and dust physics, simulations remain behind in shedding light on this point.

6. Conclusions

We present the emerging star cluster population in the barred spiral galaxy M83 using new JWST NIRCam and archival HST observations. We detect eYSCs using NIR features tracing H II regions and PDRs, and combine this with the exposed oYSCs ($\leqslant$10 Myr) detected in the HST optical bands. The main goal of this paper is to estimate the emerging timescales necessary for gas clearing and how they vary as a function of cluster physical properties and diverse galactic environment. The main findings are as follows:

1. Only a small fraction ($\leqslant$20%) of the eYSCs will probably survive as bound star clusters, while the majority are consistent with stellar associations. This is expected by observations and simulations and confirms that most star clusters may form within stellar associations.
2. The NIR colors of the eYSCs and oYSCs indicate the presence of an evolutionary sequence, from embedded to exposed. We find that the variations in the 3.3 μm PAH feature appearance (from compact to diffuse) are consistent with an evolutionary sequence where eYSCI evolve into eYSCII and to oYSCs. This sequence is clear in the F300M−F335M (tracing the excess in the 3.3 μm PAH feature) and the F115W−F187N (tracing the excess in Paα) colors, which become increasingly bluer as clusters emerge. We also find that eYSCs are younger and more attenuated than the optical counterpart and that, on average, extinction is reduced with age.
3. The mass distributions of the eYSCs and oYSCs are consistent with -2 power-law distributions. We observe variations across different galactic environments. The center and the end of the bar stand out as dynamically active regions with a high SFR, which leads to the formation of massive star clusters. We then exclude the central starburst region and analyze the disk cluster population in radial bins containing the same number of star clusters. We observe that the cluster mass function of both eYSCs and oYSCs shows similar distributions, suggesting that dynamical features such as bar and spiral arms organize star formation in the galaxy but do not enhance it.
4. Over a timescale of 10 Myr, relative numbers of eYSCI, eYSCII, and oYSCs suggest that the emergence sequence from embedded to fully exposed takes on average 6 Myr for the cluster population in M83. We find evidence that the initial embedded phase, prior to massive stars in the star cluster reaching the main sequence and starting powering their H II region, is very short. The phase over which eYSCI evolve into eYSCII and are no longer associated with 3.3 μm PAH emission lasts about 4 Myr, similar to that derived by other JWST studies (e.g., M. J. Rodríguez et al. 2023; B. C. Whitmore et al. 2023; S. T. Linden et al. 2024). After this phase, the eYSCII remain associated with an H II region only for about 2 Myr, in agreement with pre-JWST studies (e.g., M. Messa et al. 2021; S. Hannon et al. 2022). We find evidence that the emergence sequence is shorter (5 Myr) for star clusters more massive than 5000 $M_{\odot}$, while it takes on average 7 Myr for a typical cluster of a few thousand solar masses to emerge.

Overall, the recovered timescales are longer than the nominal 4 Myr assumed for SNe explosions in stellar population models (C. Leitherer et al. 2014). However, as shown by recent simulations (M. Y. Grudić et al. 2022; J. P. Farias et al. 2023), and taking into account stochastic IMF sampling (M. Chevance et al. 2022), SNe explosions in low-mass clusters of a few thousand solar masses might be delayed. This implies that the emergence sequence is mainly driven by radiative and mechanical (in the form of stellar wind) pre-SN feedback and that, at the time of the first SN explosions, their energy and momentum is injected in a processed medium, thus driving the final clearing stages.

Follow-up analysis of eYSC and oYSC populations for the entire sample of galaxies within the FEAST program will be pivotal in investigating emerging timescales in different galaxies and how they vary across a larger range of various galactic environments.

Acknowledgments

This work is based in part on observations made with the NASA/ESA/CSA James Webb Space Telescope (JWST). The data were obtained from the Mikulski Archive for Space Telescopes (MAST) at the Space Telescope Science Institute (STScI). The specific observations analyzed can be accessed via DOI: 10.17909/y4wf-yc58. STScI is operated by the Association of Universities for Research in Astronomy, Inc., under NASA contract NAS5-26555. Support to MAST for these data is provided by the NASA Office of Space Science via grant NAG5-7584 and by other grants and contracts. These observations are associated with program #1783. Support for program #1783 was provided by NASA through a grant from STScI.

This work is also based on observations made with the NASA/ESA Hubble Space Telescope and obtained from the Hubble Legacy Archive, which is a collaboration between STScI/NASA, the Space Telescope European Coordinating Facility (ST-ECF/ESA), and the Canadian Astronomy Data Centre (CADC/NRC/CSA).

This research has made use of the NASA/IPAC Extragalactic Database (NED), which is operated by the Jet Propulsion Laboratory, California Institute of Technology, under contract with NASA.

The FEAST team thanks Brent Groves for providing access to MAPPING III spectral evolutionary models. A.A. acknowledges support from Vetenskapsrådet 2021-05559. A.A. and A.P. acknowledge support from the Swedish National Space Agency (SNSA) through grant 2021-00108. A.A. and H.F.V. acknowledge support from (SNSA) 2023-00260. E.P.A acknowledges support from the NASA Astrophysics Theory Program grant 80NSSC24K0935. G.Ö. acknowledges support from the Swedish National Space Agency (SNSA). A.S.M.B. acknowledges support from the Royal Society University Research Fellowship URF/R1/191609. M.M. acknowledges financial support through grants PRIN-MIUR 2020SKSTHZ, the INAF GO Grant 2022 "The revolution is around the corner: JWST will probe globular cluster precursors and Population III stellar clusters at cosmic dawn," and by the European Union NextGenerationEU within PRIN 2022 project n.20229YBSAN "Globular clusters in cosmological simulations and lensed fields: from their birth to the present epoch." K.G. is supported by the Australian Research Council through the Discovery Early Career Researcher Award (DECRA) Fellowship (project number DE220100766) funded by the Australian Government. K.G. is supported by the Australian Research Council Centre of Excellence for All Sky Astrophysics in 3 Dimensions (ASTRO 3D) through project number CE170100013. E.S. is supported by the international Gemini Observatory, a program of NSF NOIRLab, which is managed by the Association of Universities for Research in Astronomy (AURA) under a cooperative agreement with the U.S. National Science Foundation, on behalf of the Gemini partnership of Argentina, Brazil, Canada, Chile, the Republic of Korea, and the United States of America. A.D.-C. acknowledges support from the Royal Society University Research Fellowship URF/R1/191609.

Facilities: JWST (NIRCam), HST (WFC3).

Software: astropy (Astropy Collaboration et al. 2013, 2018, 2022), Scipy (P. Virtanen et al. 2020), Source Extractor (E. Bertin & S. Arnouts 1996; K. Barbary 2016), SAOImageDs9 (W. A. Joye & E. Mandel 2003), NumPy (C. R. Harris et al. 2020), Pandas (W. McKinney 2010), Matplotlib (J. D. Hunter 2007), Seaborn (M. L. Waskom 2021).

Appendix A
Source Extraction

We report the `SEP` parameters for the source extraction and the reference image in Table A1. We refer the reader to Section 3 for guidance.

Table A1
Source Extraction Parameters for the Extraction of the eYSCs from the Continuum-subtracted F187N, F335M, and F405N, the F200W-based eYSCs, and the Optical YSCs

Source Extraction Parameter/Sources	eYSCs	F200W-based eYSCs	Optical YSCs
Reference frame	F200W	F200W	F547M and F555W
Size of background box [pixels]	30	30	30
Filter width and height [pixels]	3	1	1
Threshold pixel value	5	10	5
Minimum area of pixels	15	10	10
Number of thresholds for deblending	32	32	32
Minimum contrast ratio for deblending	0.00005	0.0005	0.0005

Appendix B
Photometric Catalogs and Advanced Data Products

The science data and catalogs used in this work are available at the Mikulski Archive for Space Telescopes (MAST) as a high-level science product via DOI: 10.17909/6dc1-9h53 and on the FEAST webpage at https://feast-survey.github.io.

Appendix C
Recovered oYSC Physical Properties over the Entire M83 Disk Observed with HST

Figure C1 shows similar plots as those presented in Figure 5 of the main text. However, we include all the optical YSCs younger than 10 Myr extracted in the HST footprints, which

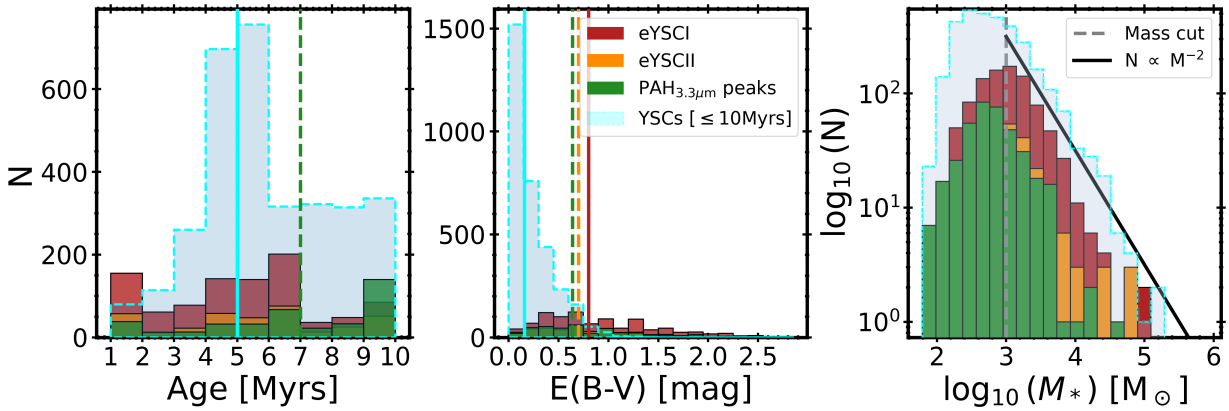

Figure C1. The stellar age (left), stellar attenuation (middle), and stellar mass distribution (right) for the different classes, eYSCI (red), eYSCII (orange), and 3.3 μm PAH peaks (green) including the oYSCs ($\leqslant$10 Myr; cyan) for the HST FOV. The vertical lines correspond to the median values of eYSCI (red), eYSCII (orange), 3.3 μm PAH peaks (green), and the YSCs ($\leqslant$10 Myr; cyan). The mass distribution (left) also includes a gray dashed line corresponding to the mass cut at $1 \times 10^3\ M_\odot$ and the black curve to the 10-logarithm of a cluster mass function (CMF) with a slope of -2. For the stellar age (left panel), the eYSCI median overlaps with the eYSCII and YSCs ($\leqslant$10 Myr).

cover an area 3 times larger than the JWST mosaic. Overall, the extended oYSCs population shows similar properties as the subsample contained within the JWST FOV. We refer the reader to Section 4 of the main text.

ORCID iDs

Alice Knutas https://orcid.org/0009-0007-2389-0332
Angela Adamo https://orcid.org/0000-0002-8192-8091
Alex Pedrini https://orcid.org/0000-0002-8222-8986
Sean T. Linden https://orcid.org/0000-0002-1000-6081
Varun Bajaj https://orcid.org/0009-0008-4009-3391
Jenna E. Ryon https://orcid.org/0000-0002-2918-7417
Benjamin Gregg https://orcid.org/0000-0003-4910-8939
Ahmad A. Ali https://orcid.org/0000-0001-5189-4022
Eric P. Andersson https://orcid.org/0000-0003-3479-4606
Arjan Bik https://orcid.org/0000-0001-8068-0891
Giacomo Bortolini https://orcid.org/0009-0003-6182-8928
Daniela Calzetti https://orcid.org/0000-0002-5189-8004
Ana Duarte-Cabral https://orcid.org/0000-0002-5259-4774
Bruce G. Elmegreen https://orcid.org/0000-0002-1723-6330
Helena Faustino Vieira https://orcid.org/0000-0002-2199-0977
John S. Gallagher https://orcid.org/0000-0001-8608-0408
Kathryn Grasha https://orcid.org/0000-0002-3247-5321
Kelsey Johnson https://orcid.org/0000-0001-8348-2671
Thomas S.-Y. Lai https://orcid.org/0000-0001-8490-6632
Drew Lapeer https://orcid.org/0009-0009-5509-4706
Matteo Messa https://orcid.org/0000-0003-1427-2456
Göran Östlin https://orcid.org/0000-0002-3005-1349
Elena Sabbi https://orcid.org/0000-0003-2954-7643
Linda J. Smith https://orcid.org/0000-0002-0806-168X
Monica Tosi https://orcid.org/0000-0002-0986-4759

References

Adamo, A., Kruijssen, J. M. D., Bastian, N., Silva-Villa, E., & Ryon, J. 2015, MNRAS, 452, 246
Adamo, A., Ryon, J. E., Messa, M., et al. 2017, ApJ, 841, 131
Adamo, A., Zeidler, P., Kruijssen, J. M. D., et al. 2020, SSRv, 216, 69
Ali, A. A., Bending, T. J. R., & Dobbs, C. L. 2022, MNRAS, 510, 5592
Ali, A. A., Dobbs, C. L., Bending, T. J. R., Buckner, A. S. M., & Pettitt, A. R. 2023, MNRAS, 524, 555
Andersson, E. P., Mac Low, M.-M., Agertz, O., Renaud, F., & Li, H. 2024, A&A, 681, A28
Astropy Collaboration, Price-Whelan, A. M., Lim, P. L., et al. 2022, ApJ, 935, 167
Astropy Collaboration, Price-Whelan, A. M., Sipőcz, B. M., et al. 2018, AJ, 156, 123
Astropy Collaboration, Robitaille, T. P., Tollerud, E. J., et al. 2013, A&A, 558, A33
Barbary, K. 2016, JOSS, 1, 58
Barbary, K. 2017, extinction v0.3.0, Zenodo, doi:10.5281/zenodo.804967
Barnes, A. T., Glover, S. C. O., Kreckel, K., et al. 2021, MNRAS, 508, 5362
Bastian, N., Adamo, A., Gieles, M., et al. 2012, MNRAS, 419, 2606
Bertin, E., & Arnouts, S. 1996, A&AS, 117, 393
Boquien, M., Burgarella, D., Roehlly, Y., et al. 2019, A&A, 622, A103
Bressert, E., Bastian, N., Gutermuth, R., et al. 2010, MNRAS, 409, L54
Brown, G., & Gnedin, O. Y. 2021, MNRAS, 508, 5935
Bruzual, G., & Charlot, S. 2003, MNRAS, 344, 1000
Callanan, D., Longmore, S. N., Kruijssen, J. D., et al. 2021, MNRAS, 505, 4310
Calzetti, D., Armus, L., Bohlin, R. C., et al. 2000, ApJ, 533, 682
Calzetti, D., Johnson, K. E., Adamo, A., et al. 2015, ApJ, 811, 75
Cardelli, J. A., Clayton, G. C., & Mathis, J. S. 1989, ApJ, 345, 245
Cerviño, M., & Luridiana, V. 2004, A&A, 413, 145
Chabrier, G. 2003, PASP, 115, 763
Chevance, M., Kruijssen, J. D., Krumholz, M. R., et al. 2022, MNRAS, 509, 272
Churchwell, E., Babler, B. L., Meade, M. R., et al. 2009, PASP, 121, 213
Corbelli, E., Braine, J., Bandiera, R., et al. 2017, A&A, 601, A146
Della Bruna, L., Adamo, A., Amram, P., et al. 2022, A&A, 660, A77
Della Bruna, L., Adamo, A., McLeod, A. F., et al. 2022, A&A, 666, A29
Deshmukh, S., Linden, S. T., Calzetti, D., et al. 2024, ApJL, 974, L24
Dobbs, C. L., Bending, T. J. R., Pettitt, A. R., & Bate, M. R. 2022, MNRAS, 509, 954
Draine, B. T. 2010, Physics of the Interstellar and Intergalactic Medium (Princeton, NJ: Princeton Univ. Press)
Draine, B. T., Aniano, G., Krause, O., et al. 2013, ApJ, 780, 172
Duarte-Cabral, A., Bontemps, S., Motte, F., et al. 2013, A&A, 558, A125
Elson, R. A. W., Fall, S. M., & Freeman, K. C. 1987, ApJ, 323, 54
Evans, N. J., II, Dunham, M. M., Jørgensen, J. K., et al. 2009, ApJS, 181, 321
Farias, J. P., Offner, S. S. R., Grudić, M. Y., Guszejnov, D., & Rosen, A. L. 2023, MNRAS, 527, 6732
Faustino Vieira, H., Duarte-Cabral, A., Smith, M. W. L., et al. 2025, MNRAS, 538, 2744
Ferland, G. J., Porter, R., Van Hoof, P., et al. 2013, RMxAA, 49, 137
Fouesneau, M., & Lançon, A. 2010, A&A, 521, A22
Fouesneau, M., Lançon, A., Chandar, R., & Whitmore, B. C. 2012, ApJ, 750, 60
Freeman, P., Rosolowsky, E., Kruijssen, J. D., Bastian, N., & Adamo, A. 2017, MNRAS, 468, 1769
Fukushima, H., & Yajima, H. 2022, MNRAS, 511, 3346
Gieles, M., & Portegies Zwart, S. F. 2011, MNRAS, 410, L6
Goodwin, S. P., & Bastian, N. 2006, MNRAS, 373, 752
Grasha, K., Calzetti, D., Adamo, A., et al. 2019, MNRAS, 483, 4707
Grasha, K., Calzetti, D., Bittle, L., et al. 2018, MNRAS, 481, 1016
Gregg, B., Calzetti, D., Adamo, A., et al. 2024, ApJ, 971, 115
Groves, B., Dopita, M. A., Sutherland, R. S., et al. 2008, ApJS, 176, 438
Grudić, M. Y., Guszejnov, D., Hopkins, P. F., Offner, S. S. R., & Faucher-Giguère, C.-A. 2021, MNRAS, 506, 2199
Grudić, M. Y., Guszejnov, D., Offner, S. S. R., et al. 2022, MNRAS, 512, 216
Gutermuth, R. A., Pipher, J. L., Megeath, S. T., et al. 2011, ApJ, 739, 84
Habel, N., Nally, C., Lenkić, L., et al. 2024, ApJ, 971, 108
Hannon, S., Lee, J. C., Whitmore, B. C., et al. 2019, MNRAS, 490, 4648
Hannon, S., Lee, J. C., Whitmore, B. C., et al. 2022, MNRAS, 512, 1294
Harris, C. R., Millman, K. J., van der Walt, S. J., et al. 2020, Natur, 585, 357
Harris, J., Calzetti, D., Gallagher, J. S. I., Conselice, C. J., & Smith, D. A. 2001, AJ, 122, 3046
Hollenbach, D., & Tielens, A. 1997, ARA&A, 35, 179
Hollyhead, K., Bastian, N., Adamo, A., et al. 2015, MNRAS, 449, 1106
Hunter, J. D. 2007, CSE, 9, 90
Janka, H. T. 2025, arXiv:2502.14836
Johnson, K. E., Indebetouw, R., & Pisano, D. J. 2003, AJ, 126, 101
Joye, W. A., & Mandel, E. 2003, in ASP Conf. Ser. 295, Astronomical Data Analysis Software and Systems XII, ed. H. E. Payne, R. I. Jedrzejewski, & R. N. Hook (San Francisco, CA: ASP), 489
Kennicutt, R. C., Jr. 1998, ARA&A, 36, 189
Kim, J., Chevance, M., Kruijssen, J. M. D., et al. 2023, ApJL, 944, L20
Kim, J.-G., Kim, W.-T., & Ostriker, E. C. 2018, ApJ, 859, 68
Kobulnicky, H. A., & Johnson, K. E. 1999, ApJ, 527, 154
Kounkel, M., Covey, K., Suárez, G., et al. 2018, AJ, 156, 84
Kroupa, P. 2001, MNRAS, 322, 231
Krumholz, M. R., Adamo, A., Fumagalli, M., et al. 2015, ApJ, 812, 147
Krumholz, M. R., McKee, C. F., & Bland-Hawthorn, J. 2019, ARA&A, 57, 227
Kuhn, M. A., Hillenbrand, L. A., Sills, A., Feigelson, E. D., & Getman, K. V. 2019, ApJ, 870, 32
Lada, C. J., & Lada, E. A. 2003, ARA&A, 41, 57
Larsen, S. S. 2004, A&A, 416, 537
Leitherer, C., Ekström, S., Meynet, G., et al. 2014, ApJS, 212, 14
Leroy, A. K., Hughes, A., Liu, D., et al. 2021, ApJS, 255, 19
Levy, R. C., Bolatto, A. D., Mayya, D., et al. 2024, ApJL, 973, L55
Lewis, S. C., McMillan, S. L. W., Mac Low, M.-M., et al. 2023, ApJ, 944, 211
Linden, S. T., Evans, A. S., Armus, L., et al. 2023, ApJL, 944, L55
Linden, S. T., Lai, T., Evans, A. S., et al. 2024, ApJL, 974, L27
Longmore, S. N., Kruijssen, J. M. D., Bastian, N., et al. 2014, in The Formation and Early Evolution of Young Massive Clusters, ed. H. Beuther et al. (Tucson, AZ: Univ. Arizona Press), 291
Maíz Apellániz, J. 2010, in IAU Symp. 266, Star Clusters: Basic Galactic Building Blocks Throughout Time and Space, ed. R. de Grijs & J. R. D. Lépine (Cambridge: Cambridge Univ. Press), 100
Maschmann, D., Lee, J. C., Thilker, D. A., et al. 2024, ApJS, 273, 14

McKinney, W. 2010, in Proc. 9th Python in Science Conf., ed. Stéfan van der Walt & J. Millman, 56
McLeod, A. F., Ali, A. A., Chevance, M., et al. 2021, MNRAS, 508, 5425
McQuaid, T., Calzetti, D., Linden, S. T., et al. 2024, ApJ, 967, 102
Menon, S. H., Federrath, C., & Krumholz, M. R. 2023, MNRAS, 521, 5160
Messa, M., Calzetti, D., Adamo, A., et al. 2021, ApJ, 909, 121
Naab, T., & Ostriker, J. P. 2017, ARA&A, 55, 59
Oey, M. S., King, N. L., & Parker, J. W. 2004, AJ, 127, 1632
Parker, R. J., Wright, N. J., Goodwin, S. P., & Meyer, M. R. 2014, MNRAS, 438, 620
Pathak, D., Leroy, A., Thompson, T., et al. 2025, ApJ, 982, 140
Pedrini, A., Adamo, A., & Bik, A. 2025, arXiv:2509.01670
Pedrini, A., Adamo, A., Calzetti, D., et al. 2024, ApJ, 971, 32
Pokhrel, R., Gutermuth, R. A., Betti, S. K., et al. 2020, ApJ, 896, 60
Polak, B., Mac Low, M.-M., Klessen, R. S., et al. 2024, A&A, 690, A94
Portegies Zwart, S. F., McMillan, S. L. W., & Gieles, M. 2010, ARA&A, 48, 431
Querejeta, M., Leroy, A. K., Meidt, S. E., et al. 2024, A&A, 687, A293
Reina-Campos, M., & Kruijssen, J. M. D. 2017, MNRAS, 469, 1282
Reines, A. E., Johnson, K. E., & Goss, W. M. 2008, AJ, 135, 2222
Rodríguez, M. J., Lee, J. C., Whitmore, B. C., et al. 2023, ApJL, 944, L26
Rodríguez, M., Lee, J. C., Indebetouw, R., et al. 2025, ApJ, 983, id.137
Ryon, J. E., Bastian, N., Adamo, A., et al. 2015, MNRAS, 452, 525
Ryon, J. E., Gallagher, J. S., Smith, L. J., et al. 2017, ApJ, 841, 92
Sirressi, M., Adamo, A., Hayes, M., et al. 2024, AJ, 167, 166
Sun, J., He, H., Batschkun, K., et al. 2024, ApJ, 967, 133
Sun, J., Leroy, A. K., Schinnerer, E., et al. 2020, ApJL, 901, L8
Tully, R. B., Courtois, H. M., Dolphin, A. E., et al. 2013, AJ, 146, 86
van der Laan, T. P. R., Armus, L., Beirao, P., et al. 2015, A&A, 575, A83
Virtanen, P., Gommers, R., Oliphant, T. E., et al. 2020, NatMe, 17, 261
Ward, J. L., Kruijssen, J. D., & Rix, H.-W. 2020, MNRAS, 495, 663
Waskom, M. L. 2021, JOSS, 6, 3021
Whelan, D. G., Johnson, K. E., Whitney, B. A., Indebetouw, R., & Wood, K. 2011, ApJ, 729, 111
Whitmore, B. C., Chandar, R., Kim, H., et al. 2011, ApJ, 729, 78
Whitmore, B. C., Chandar, R., Lee, J., et al. 2020, ApJ, 889, 154
Whitmore, B. C., Chandar, R., Rodríguez, M. J., et al. 2023, ApJL, 944, L14
Wofford, A., Leitherer, C., & Chandar, R. 2011, ApJ, 727, 100
Zackrisson, E., Rydberg, C.-E., Schaerer, D., Östlin, G., & Tuli, M. 2011, ApJ, 740, 13